UC Santa Cruz
UC Santa Cruz Electronic Theses and Dissertations

Title
Atomic layer deposition of thin films: from functional devices to protective coatings

Permalink
https://escholarship.org/uc/item/66z2d2xx

Author
Fryauf, David Mark

Publication Date
2016

Copyright Information
This work is made available under the terms of a Creative Commons Attribution License, availalbe at https://creativecommons.org/licenses/by/4.0/

Peer reviewed|Thesis/dissertation

eScholarship.org Powered by the California Digital Library
University of California

UNIVERSITY OF CALIFORNIA
SANTA CRUZ

ATOMIC LAYER DEPOSITION OF DIELECTRIC THIN FILMS: FROM FUNCTIONAL DEVICES TO PROTECTIVE COATINGS

A dissertation submitted in partial satisfaction
of the requirements for the degree of

DOCTOR OF PHILOSOPHY

in

ELECTRICAL ENGINEERING

by

David Mark Fryauf

December 2016

The Dissertation of David Mark Fryauf is approved:

____
Professor Nobuhiko Kobayashi, Chair

____
Professor Holger Schmidt

____
Andrew Phillips, Ph.D.

____
Tyrus Miller
Vice Provost and Dean of Graduate Studies

Copyright © by

David Mark Fryauf

2016

Table of Contents

List of Figures iv

List of Tables vi

List of Equations vi

Abstract vii

Acknowledgements x

Chapter 1: Introduction 1

Chapter 2: AlOx on InP nanowires 11

Chapter 3: TiO_2 memristive edge device 25

Chapter 4: PEALD barriers on Ag mirrors 32

Chapter 5: PEALD vs evaporation of AlOx barrier on Ag 43

Chapter 6: AlOx and anti-oxidation barriers on Ag 60

Chapter 7: Ion bombarded Ag 82

Chapter 8: Conclusion 102

Bibliography 104

List of Figures

Figure 1:Normalized PL spectra taken at 300K from 2 samples showing a shift in peak emission after AlOx deposition.. 13

Figure 2: Relative shift in PL peak emission (left axis) and Raman peaks (right axis) as a function of AlOx thickness.. 15

Figure 3: TEM images of (a) an original nanowire sample and (b) a nanowire with 50nm of AlOx. 18

Figure 4: Illustration of vertical RRAM device fabrication. 26

Figure 5: a) Cross-sectional SEM of a virgin 1μm device 28

Figure 6: Current – Voltage measurements of memristive switching 30

Figure 7: Schematics of the PVD samples prepared in the UCO coating chamber, with the eventual ALD oxide layer indicated 34

Figure 8: Measured reflectivity in the optical/NIR for three samples with top layers of AlOx, TiOx and HfOx 39

Figure 9: 2x2mm optical microscope images. 41

Figure 10: Schematic of samples A1 and A2 showing experimentally deposited layers. 48

Figure 11: Schematic of samples B1 and B2 showing experimentally deposited layers.. 49

Figure 12: Left: photograph of samples A1 and A2 after 231 hours of environmental stress testing. Right: Reflectivity 53

Figure 13: Same as Fig 12 but for samples B1 and B2. 55

Figure 14. Illustration showing the protected mirror film stack with 8 different various 5±1nm anti-ox materials. 64

Figure 15: Reflectivity of 16 samples before (a, b) and after environmental stressing (c, d).. 68

Figure 16: Pictures of the 16 protected mirror samples after ~10 hours of HTHH testing. 70

Figure 17. 10µm area AFM scans of a) as-deposited Ag surface and b) Ag surface after 45 seconds of Ar+ exposure. 87

Figure 18: SEM images of a) as-deposited Ag surface and b) Ag surface after 45 seconds of Ar+ ion exposure. 88

Figure 19: Reflectivity of as-deposited Ag and Ag exposed to Ar+ ion bombardment plotted with emphasis on the UV/visible spectrum features. 89

Figure 20: Protected mirror thin film stack illustration (bottom right) and resulting reflectivity spectra 91

Figure 21: Measured reflectivity curves are subtracted from the baseline calculated reflectivity curve from Fig 20 and replotted with ln x-axis.. 93

Figure 22: Illustration summarizing the Ag film microstructure (left) without and (right) with 45 seconds Ar+ exposure after Ag film deposition. 95

List of Tables

Table 1: Surface roughness parameters before and after ALD oxide growth. 35

Table 2: Fraction of damaged areas for samples A1 vs A2 and B1 vs B2. 57

Table 3: Image analysis results of 16 HTHH-tested samples. 72

Table 4: Figure of merit calculations for 16 HTHH-tested samples 80

List of Equations

Equation 1 23

Equation 2 75

Equation 3 75

Equation 4 76

Equation 5 76

Equation 6 77

Equation 7 78

Equation 8 78

Abstract

ATOMIC LAYER DEPOSITION OF DIELECTRIC THIN FILMS: FROM FUNCTIONAL DEVICES TO PROTECTIVE COATINGS

by

David Mark Fryauf

Atomic layer deposition (ALD) is a self-limiting subset of chemical vapor deposition that has become widely popular in materials science applications such as device packaging, semiconductor passivation, transistor gate dielectrics, optical coatings, and protective barriers. ALD is capable of uniformly coating high-aspect ratio features, such as 1-dimensional nanostructures or pinhole-sized vias, across a macroscopic distance which is expected to only be limited by the size of the deposition chamber. This work reviews several applications of ALD used to deposit thin conformal layers of dielectric material which specifically capitalize on the precise, conformal nature of the deposition process. Semiconductor nanowire networks coated with aluminum oxide (AlOx) by plasma enhanced ALD (PEALD) show blue-shifted photoluminescence with increasing AlOx thickness. Novel memristor "edge" devices

fabricated with an active switching layer of titanium dioxide deposited by PEALD yield an active device cross-section two orders of magnitude smaller than what is possible with conventional 2-dimensional thin film devices fabricated by similar photolithography methods. Protected silver mirrors coated with AlOx deposited by PEALD have superior durability when compared to mirrors coated with an identical layer of AlOx deposited by conventional physical vapor deposition. All of these applications benefit from the robust uniform coating properties of the ALD growth mechanism. Additional studies of dielectric barrier overlayers deposited by ALD on silver mirrors are discussed, and a figure of merit is proposed for judging overall mirror performance.

For the Knutzens – the grooviest friends

For France – my inspiration for everything that comes from my heart

Acknowledgements

This dissertation and my five years of PhD work have been made possible by the help and support of many individuals. My adviser, Professor Nobby Kobayashi, has constantly motivated my pursuit of scientific understanding and creativity. He has taught me how to be resourceful, independent, and original in a fast-paced competitive field. Dr. Andrew Phillips has become my role model of the scientific method and challenges me to be more observant in all my work. Professor Holger Schmidt's highly effective classroom teaching and prestigious academic attitude has influenced my respect for higher education. I am honored and grateful for these three influential figures that make my PhD defense committee.

I've had numerous opportunities to publish journal papers and contribute to the field of materials science through collaborations with many other professional researchers in academia and industry. I am grateful to share research with Michael Oye, Robert Cormia, and Min Wei. Previous collaboration with the prestigious quantum electronics lab at HPE Labs in Palo Alto, CA, has been possible through the mentoring and generosity of Stanley Williams, SY Wang, Byung-Joon Choi, Jianhua Yang, and Tan Ha. Several collaborative endeavors with Gary Tompa and the researchers from Structured Materials Inc. in Piscataway, NJ, have given me great experience in deposition design and the industrial environment of materials science.

Past, present, and brand new members of the NECTAR research lab group

under Prof. Kobayashi's supervision have all had a great positive impact on my learning and research. Dr. Drew Lohn and Dr. Kate Norris, two original NECTAR grads, have been exceptional mentors. I'm forever grateful for the lessons learned and memories shared with my two best friends and lab partners for five years, Dr. Junce Zhang and Juan Diaz.

The text of this thesis includes the following previously published material:

1. Fryauf, D.M., Zhang, J., Norris, K.J., Diaz Leon, J.J., Oye, M.M., Wei, M. and Kobayashi, N.P., 2014. Photoluminescence blue shift of indium phosphide nanowire networks with aluminum oxide coating. physica status solidi (RRL)-Rapid Research Letters, 8(7), pp.663-667.
2. Fryauf, D.M., Norris, K.J., Zhang, J., Wang, S.Y. and Kobayashi, N.P., 2015. Titanium oxide vertical resistive random-access memory device. IET Micro & Nano Letters, 10(7), pp.321-323.
3. Fryauf, D.M., Phillips, A.C. and Kobayashi, N.P., 2013, September. Moisture barrier and chemical corrosion protection of silver-based telescope mirrors using aluminum oxide films by plasma-enhanced atomic layer deposition. In SPIE NanoScience+ Engineering (pp. 88200Y-88200Y). International Society for Optics and Photonics.
4. Fryauf, D.M., Phillips, A.C. and Kobayashi, N.P., 2015. Corrosion barriers for silver-based telescope mirrors: comparative study of plasma-enhanced atomic layer

deposition and reactive evaporation of aluminum oxide. Journal of Astronomical Telescopes, Instruments, and Systems, 1(4), pp.044002-044002.

5. Fryauf, D.M., Diaz Leon, J.J., Phillips, A.C. and Kobayashi, N.P., 2016. Performance of silver mirrors protected with evaporated anti-oxidation layers and ALD aluminum oxide barrier overlayer. Journal of Astronomical Telescopes, Instruments, and Systems (submitted 12/2016, under review).

6. Fryauf, D.M., Diaz Leon, J.J., Phillips, A.C. and Kobayashi, N.P., 2016. Silver film surface diffusion suppression by ion bombardment decreases surface plasmon resonance absorption. Journal of Applied Physics (submitted 12/2016, under review).

Chapter 1

Introduction

1.1 Atomic Layer Deposition Process

Thin films of metal, semiconductors, and insulators of both organic and inorganic material are fundamental to the functionality of virtually every field of technology. Any electronics, including modern computers, using microprocessors rely on thin film deposition to create the billions of transistor and capacitor devices, and Moore's Law progresses because of intensive research efforts to further understand and optimize thin film deposition techniques in device fabrication[1,2]. Modern flat screen displays are illuminated by arrays of liquid crystal displays or light emitting diodes which are all fabricated and packaged with thin film deposition of various methods[3]. Specialized construction materials, tools, and precision mechanical components are often coated with protective barrier materials by a thin film deposition[4]. Even the food processing and packaging industry heavily utilizes such deposition techniques[5]. The scope and abilities of deposition methods continues to advance, and each method has unique strengths for specific applications. This dissertation highlights the strengths of a particular method of thin film deposition,

atomic layer deposition (ALD), by demonstrating several specific applications which highlight the capabilities of ALD. Each application analyzes the thin film properties which are optimized or can only be achieved by ALD.

ALD is defined as a subset of chemical vapor deposition (CVD). CVD is a vacuum-based deposition method combining reactants to form a product in gas phase which adheres to the desired substrate. Unlike physical vapor deposition methods in vacuum, deposition can occur at higher pressures/lower vacuum (~mTorr to ~100Torr)[6]. Gaseous reactants travel to the substrate in the deposition chamber by conventional fluid flow dynamics and diffusion rather than line-of-sight mechanics. Dynamic equilibrium during CVD is a complex balance of partial pressures of the incoming reactants, the newly formed products, the byproducts, and vacuum pressure and volume flow around the specific chamber and substrate shape. CVD reactions can also differ from other conventional chemistry processes and molecular beam epitaxy by using synthesized organic molecules to carry desired reactants so that heavy materials, such as metals, can be introduced into a vacuum chamber for vapor reaction. Such synthesized organic "carrier" molecules for metals are called metal-organic precursors, and CVD using these reactants is referred to as metal-organic chemical vapor deposition (MOCVD). The dynamic equilibrium of MOCVD chemical reaction in vacuum is then further complicated by the organic byproducts of the metal-organic carrier molecules and the additional step required to "crack" these molecules in order to separate the desired metal atom reactant from the organic molecular structure. The MOCVD process is the most common deposition method for

high-quality III-V semiconductor growth for devices such as solar cells[7], LEDs[8], and high-electron-mobility transistors[9]. However, it is a complex process with many interdependent growth parameters which must be highly refined and carefully controlled for consistent growth.

ALD relies on the same chemical procedures and reaction mechanisms of CVD without the need for the careful reaction dynamic equilibrium balancing. Instead of introducing both reactants simultaneously into the deposition chamber, ALD exposes the chamber and substrate to each chemical reactant sequentially and exclusively in a step-by-step process[10,11]. Excess reactants are purged to the vacuum exhaust between each reactant exposure in order to limit excess product formation in the gas phase subject to fluid flow dynamics. This sequential discrete cycle of reactant introduction ideally creates a self-limiting chemistry that forms chemical products uniformly across every surface in vacuum. When only one reactant is introduced at a time, the reactant adheres to every surface in the chamber, including the substrate, even those with extremely complex surface features. When adhesion between the reactant and the substrate surface is stronger than the cohesion between similar reactant molecules, which is the designed property of the commonly-used metal-organic precursors, only one monolayer of the reactant is able to adhere to the substrate surface in vacuum. All excess precursor reactant molecules which don't adhere to a surface within the chamber are removed via vacuum exhaust in the purge step of the cycle. After purging the all excess of one reactant (A) from the chamber, the second reactant (B) is introduced. The maximum chemical reaction can now only

occur with the available monolayer of the first reactant A adhering to the substrate surface. In the step of introducing the second reactant B, only one monolayer of the product (C) can form in the same conformally covered area as the monolayer of A originally covered. Upon purging the excess reactant B, one ALD cycle is complete, and one monolayer of C remains uniformly on every surface in the chamber. This cycle of discrete steps is then repeated to obtain the desired thickness of thin film product C on the substrate with a linear growth rate dependent on number of cycles.

Maintaining ideal ALD growth requires complete but not excessive saturation in each of the four steps of the cycle. Adequate amounts of reactant vapor must be introduced to the chamber in order to cover every surface. Enough time must be given for each purge cycle to completely remove excess reactant. Adding too much reactant requires a longer subsequent purge step in order to remove excess. Excessive purge time increases the chances of trace reactants adhered to a surface to desorb and be purged, leaving a sub-monolayer of reactant coverage on the surface. If parameters of any of the four steps are not saturated, then the growth rate will not be conformal or not follow a simple linear dependence on number of cycles. However, when the parameters of each step are driven to adequate saturation, the growth is considered to be within the "ALD window" which produces consistent conformal growth of thin films, even if parameters of the individual steps vary slightly but remain saturated. The saturation levels vary between each reactant precursor, different deposition chamber designs, pressure, and temperature. Therefore, for each unique ALD

process, deposition parameters must be explored to ensure that growth falls within the ALD window.

1.2 Semiconductor nanowires

Nanostructures develop unique properties which are not seen in the traditional bulk samples as feature sizes scale down. When the dimension of the features shrinks into the tens of nanometers or less, within the same magnitude of the De Broglie wavelength of the charge carriers, quantum confinement occurs with an altered density of states (DOS). Nanowires (one-dimensional or 1-D structures) are an excellent example of the unique and interesting characteristics not seen in bulk materials[12]. Electrons in nanowires are confined laterally across the nanowire radius and occupy different discrete quantum energy levels, different from the continuum energy bands in bulk materials. Nanowire materials have been applied to a wide range of electronic, optical and mechanical applications, including thermoelectric applications[13]. Semiconductor nanowires (SNWs) of Group IV (e.g. silicon) and many different Group III-V compound (e.g. indium phosphide) semiconductor nanowires have been demonstrated[14,15].

In nearly all of these potential applications for SNWs, the precise control of optical properties is vital to designing optoelectronic devices. Many physical properties of SNWs, including optical properties such as photoluminescence (PL), are strongly associated with specific structural and geometrical properties of SNWs. It

has been shown that PL peak energy depends directly on the size[16] and crystallographic structure[17] of SNWs. A variety of techniques exist for growing SNWs, including atomic layer deposition, molecular beam epitaxy, chemical beam epitaxy, and metallorganic chemical vapor deposition (MOCVD)[18,19]. These different techniques yield SNWs with a wide range of structural morphology and result in a variety of optical properties. For SNWs, tuning of growth processes for desirable optical properties is therefore complicated and often not reproducible due to unavoidable fluctuations in thermodynamics of growth environments and competing growth kinetics. A simple post-growth fabrication step utilizing ALD allows for additional control of PL peak energy in SNWs which could be applied to many semiconductor nanostructures fabricated by different techniques (Chapter 2).

1.3 Memristor devices

Leon Chua's theoretical discovery of the memristor circuit element in 1971[20,21] began the search for a practical material system which displays memristive electrical characteristics. It has the potential to revolutionize computing with application for non-volatile random access memory, dynamic random access memory, and flash memory[22,23,24]. Memristor implementation in data routing networks and neuromorphic brain-mimicking networks has also been discussed[25,26]. Resistive memory characteristics were demonstrated by Chen et al. from Spansion LLC using cuprous oxide switching material in a metal-insulator-metal (MIM)

structure[27]. Williams et al. from HP Labs also realized a non-volatile switching material system in 2006 using a two-terminal Pt/TiO2/Pt stack[28]. Since this recent revival of Chua's pursuit of a memristor circuit element, memristive switching, often called resistive RAM (RRAM) behavior, has been identified in a variety of other materials systems[29,30]. Chua's recent review of memristors[31] highlights the evolution of memristive systems beginning with pre-historic jellyfish ion channels found from fossil records, then Chua's theoretical discovery in 1971, finalized by HP Labs' successful nanoscale memristor fabrication and then synthesis of a single-molecule memristor at Karlsruhe Technical University.

The vacancy drift mechanism understood in HP Labs' MIM material system[32,33] has driven a significant amount of novel studies in fabrication, characterization, and application of metal oxide-based memory materials systems. Transition metal oxides have attracted interest in memory devices due to structural simplicity, high-density integration, fast switching, and low power consumption. RRAM devices based on TiO2, which shows superior non-volatile switching behavior[34], have been fabricated using a variety of methods including solution-based processing on flexible substrates[35], electrohydrodynamic inkjet printing[36], and nanoimprint lithography (NIL)[37]. Ella Gale's recent review of TiO2 devices presents the most current comparison of switching mechanisms, modeling, and the overlapping TiO2-based research in the memristor and RRAM fields[38]. However, the quest for smaller devices continues, as the vacancy drift mechanism has been accurately modeled and experimentally proven to occur in a device with an active

switching area much smaller than features easily obtained by conventional photolithography. For instance, extensive studies of TiO2-based RRAM switching mechanisms by atomic force microscopy (AFM) and transmission electron microscopy (TEM) have revealed that switching channels form within a ~1nm radius, and TiO2 devices have been fabricated with active areas as small as 50x50nm to observe these mechanisms[39]. Conducting channel cross sections in the order of 1nm make it difficult to find and study switching mechanisms within larger devices fabricated by conventional photolithography. Additionally, formation and switching current has been observed to scale with device active area due to a proportional increase in the number of conducting channels[40].

We further explore materials systems for vertical RRAM devices and report fabrication of unique TiO2 devices with active area cross sections an order of magnitude below the limits of conventional photolithography. Baek et al. from Samsung Electronics Co. realized TaOx-based vertical multi-stack memory devices by modifying their existing vertical NAND process and architecture in 2011[41]. Subsequently, vertical multi-stack RRAM devices were fabricated with active switching materials including WOx[42], HfOx[43], and TaOx/TiO2[44]. Our work studies the feasibility of vertical sidewall memory cell fabrication with TiO2 active switching material deposited by PEALD. ALD is a practical deposition method for small features of memory device fabrication due to its conformal coverage of many materials at high aspect ratios. We have chosen to study the vacancy drift mechanism of resistive switching observed by Williams et al. in the novel vertical sidewall

structure by fabricating Pt/TiO2/Pt memory cells using e-beam deposition of contact electrodes, PEALD of TiO2 switching material, and conventional photolithography and wet etching (Chapter 3).

1.4 Silver-based telescope mirrors

Durable broad-band silver-based mirrors have long been a goal for astronomical telescopes. Silver's higher reflectivity and low emissivity in the thermal IR have significant performance benefits over the standard aluminum mirror coatings currently in widespread use. There have been some qualified successes for silver coatings – notably that used on the Gemini telescopes[45,46,47]– but the fact that so few ground-based telescopes have Ag-based coatings demonstrates the elusiveness of the goal. Many coatings that seem to hold up in the laboratory do not endure well when exposed to an actual observatory environment. Even the successful Gemini coating comes at a cost of sacrificing the deep blue and UV portions of the spectrum, an unacceptable compromise for many astronomical research programs. The University of California Observatories (UCO) has undertaken a program to develop and/or identify high-performance coatings useful for astronomical optics (Phillips et al.[48,49,50]). A strong motivation for this project is to develop and/or identify protected-Ag mirror coatings that meet the requirements of the Thirty-Meter Telescope (TMT) project, which requires high reflectivity from $0.34 < \lambda < 28\mu m$[51].

Silver itself is a relatively easy material to deposit but bare Ag quickly tarnishes (mostly due to oxidation with sulfur compounds) or forms salts with halides. Thus, to provide a long-lasting mirror coating, silver must be protected by barrier layers of transparent dielectrics in order to prevent tarnish and corrosion. The design of these barrier layers has several constraints, and identifying suitable materials and deposition processes has proven challenging. Phillips et al. discuss in some detail the constraints and challenges. They also report that certain materials, notably YF3 in combination with high-index oxides, seem promising.

Telescope mirrors have traditionally been coated by physical vapor deposition (PVD) techniques. However, the large areas of these mirrors and non-cleanroom environment during substrate cleaning and coating means that pinholes can be a significant problem, providing moisture and other chemicals a means to enter the coating and cause corrosion. Atomic layer deposition (ALD), being conformal, holds the promise of pinhole-free barrier layers. While ALD is a defined subset of chemical vapor deposition techniques, it is specifically advantageous for deposition processes requiring low temperatures, especially when the reactant gas is ignited into a plasma, which is known as plasma enhanced ALD (PEALD). Furthermore, the low-stress, amorphous nature of ALD films night be expected to improve durability as well. The excellent thickness uniformity achievable with ALD is another benefit. Chapters 4-7 focus on the experimental reflectivity and durability achieved with ALD barrier overlayers for protected Ag films.

Chapter 2

Blue-shifted photoemission of indium phosphide nanowires coated with aluminum oxide by plasma enhanced atomic layer deposition

This paper describes our finding that optical properties of semiconductor nanowires were modified by depositing a thin layer of metal oxide. Indium phosphide nanowires were grown by metal organic chemical vapor deposition on silicon substrates with gold catalyst resulting in three-dimensional nanowire networks, and optical properties were obtained from the collective nanowire networks. The networks were coated with an aluminum oxide thin film deposited by plasma-enhanced atomic layer deposition. We studied the dependence of the peak wavelength of photoluminescence spectra on the thickness of the oxide coatings. A continuous blue shift in photoluminescence spectra was observed when the thickness of the oxide coating was increased. The observed blue shift is attributed to the Burstein-Moss effect due to increased carrier concentration in the nanowire cores caused by repulsion from intrinsic negative fixed charges located at the inner oxide surface. Samples were further characterized by scanning electron microscopy, Raman

spectroscopy, transmission electron microscopy, and selective area diffractometry to better understand the physical mechanisms for the blue shift.

2.1 Experimental Procedure

Photoluminescence of networks of indium phosphide nanowires (InPNWs) has been measured at room temperature before and after the deposition of aluminum oxide (AlOx) thin films deposited by plasma enhanced atomic layer deposition (PEALD). Indium phosphide (InP) has been chosen as a material for nanowires because it is known to have a surface state density much lower than that of other group III-V compound semiconductors, which offers advantages in studying photo emission resulting from radiative recombination of photo generated electron-hole pairs[52] at room temperature. AlOx has been chosen as the post-growth coating due to the extensive understanding, development, and simplicity of the surface chemistry in the self-limited reaction by PEALD which creates highly uniform conformal films in a variety of material systems[10]. A clear trend in the PL response of these InPNWs has been observed to be explicitly dependent on the thickness of AlOx deposited by

PEALD; as film thickness increases, the peak photo emission shifts to higher energy.

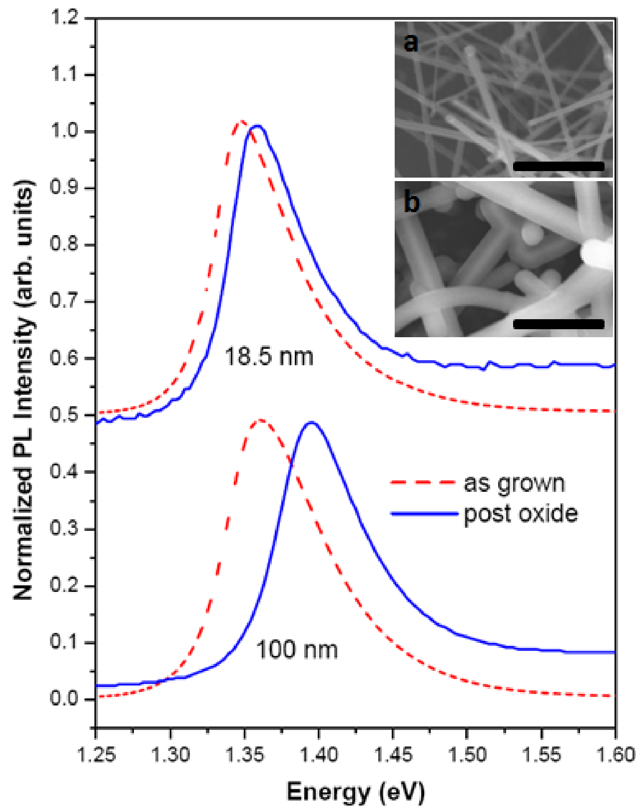

Figure 1:Normalized PL spectra taken at 300K from 2 samples showing a shift in peak emission after AlOx deposition. The inset shows a) original nanowires and b) nanowires after 100nm of AlOx with the scale bars representing 1µm.

The InPNWs were grown by MOCVD using trimethylindium and di-tert-butylphosphine as indium and phosphorous precursors, respectively. The growth was nucleated on n-type Si(100) which was previously etched in a buffered hydrofluoric acid solution for 1 minute to remove native oxide and then drop-casted with a colloidal solution of 50nm gold nanoparticles as catalyst. The nanowires grew with the axis of growth along the InP<111> direction, in random directions, which created a network of InPNWs, shown in Fig. 1a. The samples were then analyzed by

scanning electron microscopy (SEM) and PL mapping to check for consistency across each 0.25cm^2 sample. All shift in emission discussed in the results of this experiment are relative to the original emission of each individual sample. We have also chosen to study the collective properties of large ensembles of nanowires rather than the properties of individual nanowires, and all the resulting spectra in this report are measurements of approximately 1mm diameter areas of InPNWs, which corresponds to the PL excitation beam spot size.

After initial characterization, the as-grown samples were coated with various thicknesses of AlOx using an Oxford FlexAl ALD system with an inductively coupled plasma source. AlOx was deposited at 150°C using trimethylaluminum and oxygen gas for the aluminum precursor and reactant oxidizer, respectively. Deposition rates and film thicknesses were previously calibrated using ellipsometry. 8 samples were made with 8 different AlOx thicknesses ranging from 8nm to 100nm. PL was measured before and after the ALD growth, and relative peak shift was measured. The sample with 50nm of oxide and an uncoated sample were selected for transmission electron microscopy (TEM) and selective area diffraction (SAD) analysis.

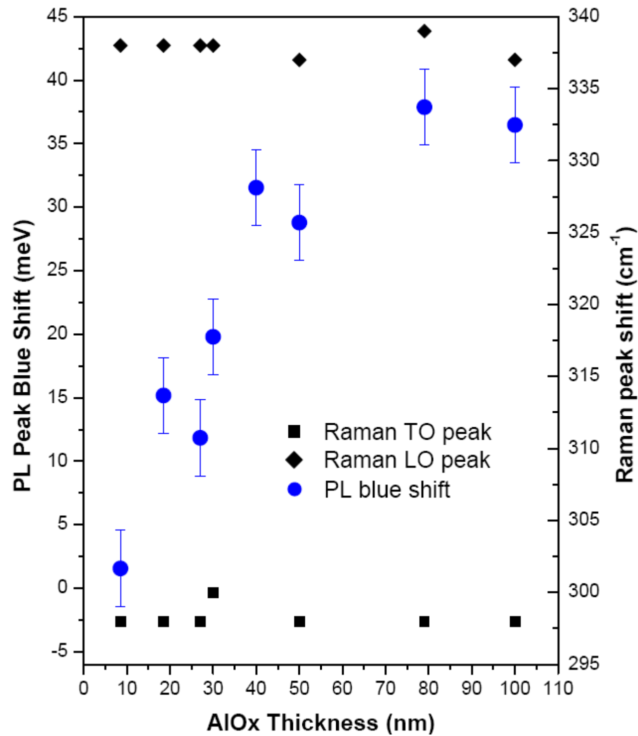

Figure 2: Relative shift in PL peak emission (left axis) and Raman peaks (right axis) as a function of AlOx thickness. Vertical bars indicate systematic error in PL measurements.

Photoluminescence measurements were taken from an arbitrary spot defined by a pinhole mask applied to the sample with an approximate spot size equal to the PL excitation beam diameter (~1mm). After being coated with AlOx by ALD, this same arbitrary spot was measured again. Fig. 1 shows comparative spectra of two samples coated with 18.5nm and 100nm of AlOx, respectively. Each PL spectrum has been normalized with respect to its original peak intensity so that the spectral profiles can be compared. It is apparent that the spectral profile shows virtually no change in both of these examples. The sample coated with 18.5nm AlOx shows

approximately 15meV blue shift in peak energy, while the sample coated with 100nm AlOx shows approximately 36meV blue shift.

The dependence of blue shift in PL peak energy on deposited AlOx thickness for all eight samples is plotted in Fig. 2. The error measurements represent a systematic approximate 1.5meV variation in PL spectra, which is doubled to account for both pre-oxide deposition and post-oxide deposition measurements on each sample. The scatter plot data suggests saturation beyond 90nm of deposited AlOx with a 35meV blue shift being the approximate maximum shift.

The as-grown nanowires and the sample with 50nm of AlOx were analyzed with TEM for a comparison in structural properties and lattice constants. TEM images confirmed the expected thickness of AlOx being grown by ALD, and it allowed us to perform SAD measurements in an attempt to assess the presence of residual strain in the InPNW lattices. Fig. 3a shows an as-grown nanowire, and Fig. 3b shows a nanowire with 50nm of AlOx coating. SAD measurements of each sample are inset. From the SAD patterns, it is found that the lattice constants along InP[111] and overall crystallographic symmetry of each sample are virtually identical, which indicates that the crystallographic structure of InPNWs is not affected by strain associated with the deposited AlOx layers.

Raman spectroscopy was performed on the as-grown InPNW samples and all samples after oxide deposition in an attempt to confirm the conclusion that strain-induced bandgap widening is not the primary contribution to the PL blue shift. Spectra were collected at room temperature using a JY-Horiba spectrometer with a

632nm excitation laser under 100x magnification. Characteristic Raman shift peaks representing the transverse optical (TO) and longitudinal optical (LO) phonon modes of bulk InP were identified at 298 cm^{-1} and 338 cm^{-1}, respectively. The relative shift between each phonon mode of all samples was analyzed for any trend which would account for the observed blue shift with increasing oxide thickness. Fig. 2 shows the relative shift of these two peaks as a function of deposited AlOx thickness on the right vertical axis. No trend in relative peak shift can be observed from the scatter plot. Fig. 3c shows Raman spectra of the as-grown nanowires, 18.5nm-coated sample, and 100nm-coated sample with no observable shift.

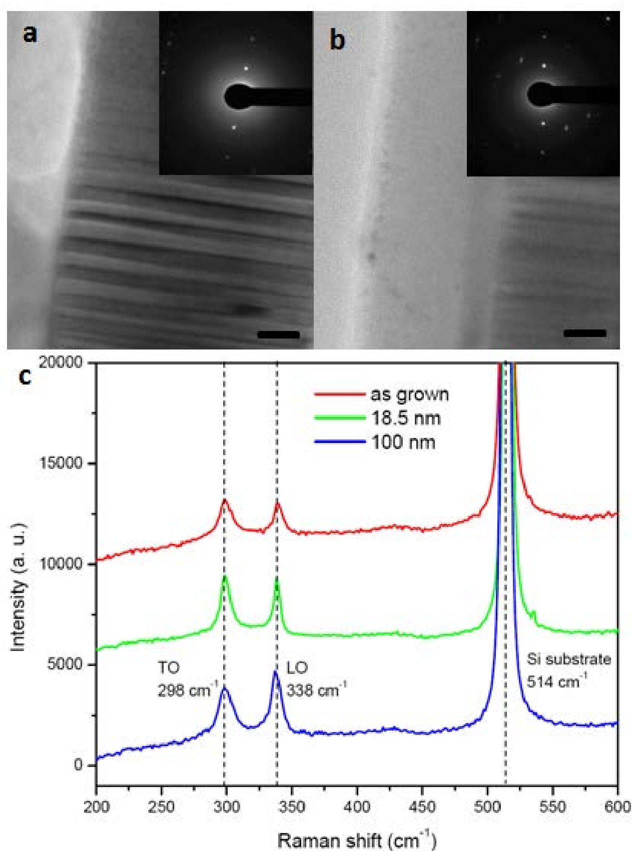

Figure 3: TEM images of (a) an original nanowire sample and (b) a nanowire with 50nm of AlOx. The SAD of each image is inset. The scale bar represents 20nm. Raman spectra (c) are shown for the as-grown sample and 2 other samples to demonstrate the negligible shift in bulk InP phonon modes. The TO and LO modes (298 cm^{-1} and 338 cm^{-1}, respectively), along with the characteristic bulk silicon peak (514 cm^{-1}) are shown by vertical dashed lines.

2.2 Discussion

From the trend shown in Fig. 2, we can conclude that there is an evident correlation between the amount of the blue shift and the thickness of AlOx deposited by ALD. Fig. 2 suggests a point of saturation (~90nm AlOx thickness) beyond which

the increase in blue-shift appears to dramatically slow down with greater AlOx thickness. The relationship between deposited oxide thickness and the blue shift, in addition to the possible saturation region in Fig. 2, offers some insight into the shift physical mechanisms.

Several possible mechanisms have been discussed in previous work in an attempt to explain the blue shift[53]. One possibility discussed is structural change to the InPNW during the ALD process. InP can crystallize with both zinc blend and wurtzite crystal structures in the form of nanowires[54]. The uncoated InPNWs in our experiment exhibit PL spectra consistent with those expected for zinc blend InPNWs suggesting that uncoated InP nanowires in our experiment possess zinc blend structures[55]. It has been observed that wurtzite InPNWs have bandgap energies at least 68meV larger than zinc blend InPNWs[56], and the range of wurtzite InPNW bandgap energies is larger than those measured on the coated nanowire networks in our experiment. For instance, as shown in Fig. 1, the 100nm sample, the thickest AlOx coating, peaks at 1.40eV, which is substantially lower energy than the peak emission energy (~1.43eV) expected for wurtzite InP nanowires[55]. Furthermore, it is highly unlikely that the transition from zinc blend to wurtzite crystal structure occurs at temperatures as low as 150°C used for the ALD. If wurtzite InP was locally present within zinc blend InPNWs, then the two types of PL emission spectra would have overlapped in the spectra collected after the AlOx deposition. Fig. 1 explicitly shows the preserved shape of the PL emission before and after the AlOx deposition, which suggests that contribution from wurtzite InPNWs to the blue shift is not valid.

Another possible mechanism is that aluminum diffuses into the InP lattice and forms indium-aluminum phosphide (InAlP) ternary compound semiconductor. This is also expected to be improbable for the same reasons; the ALD process was done at 150°C, which is not hot enough to drive aluminum into the nanowire lattice when there is roughly an order of magnitude difference between the heat of formation of aluminum oxide and aluminum phosphide[57].

Lattice strain, in particular compressive biaxial strain perpendicular to the long axis of nanowires, is another feasible mechanism for the blue-shift. However, the TEM analysis disproves this possibility. It is clear, from the virtually identical [111] lattice diffraction spacing of both samples in Fig. 3a and 3b, that the f.c.c. lattice is not strained by the deposition of AlOx. The low deposition temperature of the AlOx can also account for this lack of strain in the system. In ALD processes, amorphous AlOx grows at temperatures under 600°C[58], and the lack of crystallographic lattice in amorphous AlOx also reduces the possibility of strain-induced bandgap widening that would have caused the blue shift.

Raman spectroscopy measurements provide further evidence that lattice strain is not responsible for the observed blue shift. Previous observations of similar semiconductor systems under Raman analysis have shown that strain-induced bandgap widening can be accurately modeled and experimentally confirmed using Raman spectroscopy[59]. Our InPNWs exhibited virtually no shift in the two bulk InP Raman peaks regardless of different oxide thicknesses. Scatter plot data in Fig. 2 shows that the Raman peak positions have no dependence on deposited AlOx

thickness. Two Raman spectra were selected for comparison with the as-grown InPNW sample in Fig. 3c, and no relative shift can be observed. This enforces our conclusion that lattice strain, if it is present, has negligible contribution to the PL blue shift.

We assume that the nanowires coated with AlOx experience uniform fixed negative charges present at the nucleating surface of the oxide, and the resulting Coulombic repulsion confines electrons within a smaller diameter of the InPNWs. Recorded observations of charge effects during ALD growth of AlOx verify the assumption that negative fixed charges are likely to be present[60,61]. This is explained by Shin as a stoichiometric imbalance during the nucleation and initial monolayers of AlOx growth in which the initial monolayers become oxygen-rich and negatively charged, and the charges are balanced within the remaining "bulk" of AlOx as an ALD process continues[61]. The assumption of decreasing the effective conducting diameter of the InPNWs to a size within the Bohr radius of InP (~15nm[62]), however, is difficult to comprehend. Fig. 1 displays nanowires with diameters close to 100nm, which is significantly larger than previously observed InPNWs experiencing quantum confinement[16]. While our observed blue shift does seem to increase with an increase in the assumed fixed charge layer (relative to AlOx thickness), the trend of Fig. 2 PL shift does not correlate to the inverse square relationship between band energy and effective radius which is inherent in the equation for a cylindrical quantum well. Previously observed blueshift in InP nanowires of smaller diameter have also displayed the characteristic PL peak broadening of 1-dimensional structure density of

states[16], while our observed blue shifted PL spectra does not exhibit any peak broadening or shape change. Therefore, the observed blue shift in our experiment cannot be simply attributed to quantum confinement.

The negative fixed charge formation on the nucleating surface of the AlOx deposited by ALD is still a valid assumption, and we propose to attribute our blue shift to the Burstein-Moss effect. If a uniform conformal AlOx layer with embedded negative charges exists around the circumference of the InPNWs, then Coulombic repulsion creates a potential gradient from the outer diameter to the center of each nanowire uniformly along the axis. Electrons repelled by the fixed charges provided by the AlOx become concentrated towards the cores of the nanowires and leave some portion of the outer diameters depleted of electrons and more concentrated with holes. This effectively raises the electron quasi-Fermi level into the conduction band and lowers the hole quasi-Fermi level into the valence band, thus increasing the absorption energy edge and effective bandgap towards the center of the nanowire. As carrier concentration increases with decreasing volume for free electrons, the Fermi level rises into the conduction band. Electrons fill the lower energy states within the conduction band thus forcing photo-generated electron-hole pairs to separate and recombine over a significantly higher energy gap which blue-shifts photoemission from radiative recombination[63].

Liu et al.[64] has demonstrated InPNWs grown on Si substrates by the vapor phase transfer method and doped with various donors, and they found that the PL peaks blue shifted for nanowires with measured carrier concentrations within the

range of 5 e^{17} cm^{-3}. Using the equation

Equation 1

$$\Delta E = 16.9 \times \frac{m_o}{m} \times \left(\frac{n}{10^{19} cm^{-3}}\right)^{\frac{2}{3}} (meV)$$

to estimate Burstein-Moss shift, we found that our measured blue shift energies correlate to carrier concentrations between 1 e^{17} cm^{-3} and 8 e^{17} cm^{-3}. This range of increasing carrier concentration correlates well with the assumed decreasing radius of free electrons within the InP nanowires. Simiar studies of InPNWs with PL peaks blue shifted by the Burstein-Moss effect[65,66] have shown that semiconductors with low effective electron mass, such as InP (.08m_o), can achieve Fermi level shifts into the conduction band at relatively low carrier concentrations. Therefore, we assume that our unintentionally doped InPNWs have carrier concentrations within a range that can be modulated by carrier confinement caused by Coulombic repulsion from fixed charges at the nucleating surface of AlOx deposited by PEALD.

We believe that the InPNWs examined in this experiment are subject to the Burstein-Moss shift mechanism according to the experimental trend shown in Fig. 2. As AlOx thickness increases on InPNW samples, the fixed charge layer accumulates to a certain saturated magnitude which relates to a certain saturated bandgap increase within the InPNWs. Therefore, we attribute the saturation of the experimental trend in Fig. 2 to the maximum amount of fixed charge forming in the AlOx layer deposited by ALD. We consequently assume that the fixed charge formation increases non-

discretely as AlOx thickness increases, and the resulting trend of increasing PL emission blue shift is directly related to the increasing confinement of electrons within a decreasing diameter around the center part of the InPNWs. Further study of the fixed charge magnitude of AlOx by ALD is necessary to quantitatively relate PL emission blue shift to AlOx deposition thickness for the InPNW/AlOx interface. Understanding this blue shift trend may lead to accurate modeling of a variety of nanostructured semiconductor/oxide material systems, which can enable post-growth photoemission tuning of optoelectronic semiconductor devices for many applications.

Chapter 3

Titanium dioxide edge device memristors

Pt/TiO_2/Pt vertical resistive RAM switching devices were fabricated in a vertical 3D structure by combining conventional photolithography, electron-beam evaporation for electrodes, and atomic layer deposition for dielectric layers. The active switching cross-sectional area was approximately 0.02μm^2, which is comparable to nano-sized devices that require more elaborative fabrication processes. Structural integrity and electrical characteristics of the vertical memory device were analyzed by cross-sectional scanning, transmission electron microscopy, and current-voltage characteristics.

3.2 Experimental procedure

Memristive edge devices were fabricated as follows. A silicon wafer with 200nm thermal oxide was cleaned with organic solvents and spin coated with double layer photo resists measuring 200nm and 800nm for a combined 1µm photo resist layer. UV lithography was performed using a crossbar device mask with bar widths of 1µm and contact pads of 100μm^2. After developing the photo resist, the wafer was patterned with recessed openings in the photo resist layer, the bottom electrode stacks were deposited on the thermal oxide through this recess pattern. E-beam evaporation

at 1x10-6 torr was used to deposit the following stack from bottom to top: 50nm Al_2O_3, 1nm Ti for adhesion (not shown in Fig. 4), 10nm Pt, and 100nm Al_2O_3. Liftoff was subsequently performed followed by rinsing with organic solvents and 30 seconds of de-scum RIE using O_2 plasma. The resulting patterned stack (i.e., bottom electrode stack) is illustrated in Fig. 4a.

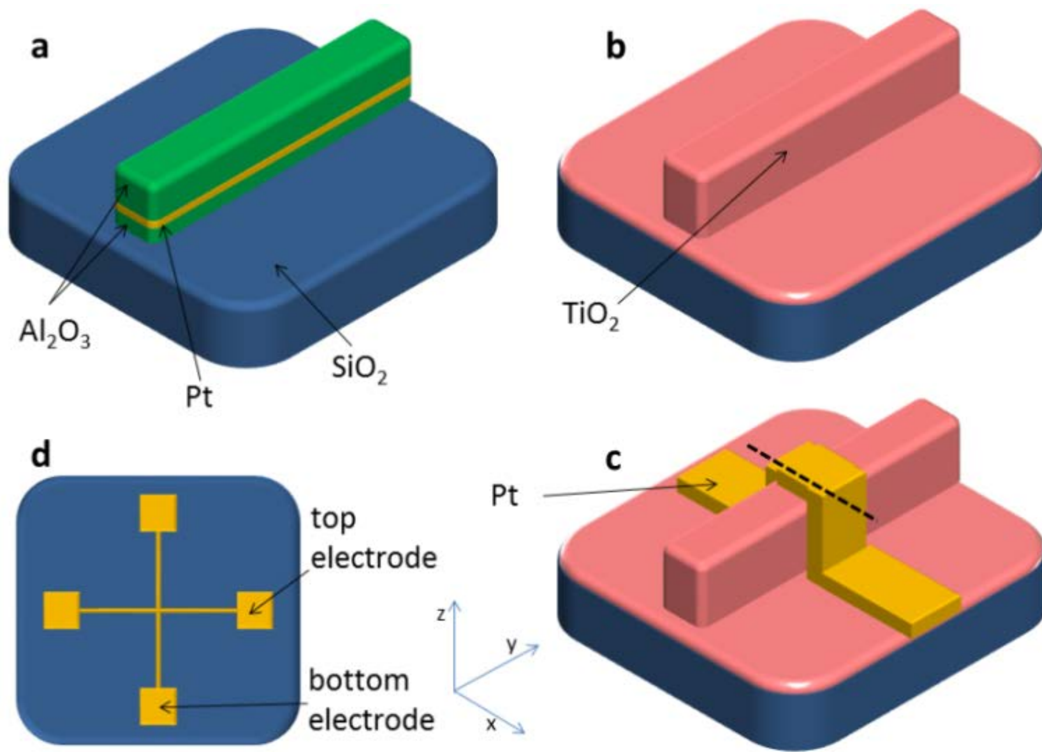

Figure 4: Illustration of vertical RRAM device fabrication (not drawn to scale). In frame a) from bottom up: SiO_2 substrate, 50nm Al_2O_3 dielectric spacer, 10nm Pt bottom contact, 100nm Al_2O_3 dielectric spacer. In b) uniform 5nm TiO_2 switching layer is added, and in c) 50nm Pt top electrode is added. Black dashed line indicates the 2D area of the x-z plane shown in the corresponding XSEM in Fig 5a. Frame d) illustrates crossbar device structure with 1µm-wide bars and 100µm contact pads (not drawn to scale).

The 5nm TiO_2 switching layer was then deposited by PEALD at 300°C using $TiCl_4$ and O_2 precursors for the titanium and oxygen reactants, respectively. The TiO_2 layer conformally covered the wafer including the bottom electrode stack as illustrated in Fig. 4b. A similar photolithography process with a single resist layer was then repeated to put the same crossbar pattern orthogonally on top of the existing bottom electrode stack covered with an ALD-deposited TiO_2 switching layer. E-beam evaporation at 1x10-6 torr was used again to deposit 2nm Ti (not shown in Fig. 4) and 50nm Pt for the top electrode stack, which was followed by final liftoff and rinsing with organic solvents, as illustrated in Fig. 4c. A top view of the fabricated memristive edge device is illustrated in Fig. 4d.

Cross-sectional SEM and TEM with FIB were used to study structural integrity of the device and compare the fabricated device to its design. Fig. 5a shows the SEM cross section taken across the 1µm-wide bottom electrode stack at the intersection of the top electrode stack as indicated by the black dashed line in Fig. 4c. Fig. 5b is a TEM image of one side of a device with stack materials labeled. Fig. 5c is a magnified TEM image where switching is expected to occur between the top and bottom Pt electrodes with the TiO_2 layer in between. Device IV curves were collected with an Agilent semiconductor parameter analyzer using the 4 point probe method for electrical characterization. IV measurements were done with a bipolar DC sweep from -2V to +2V with a compliance current set at 5µA. A representative bipolar memristive switching curve is shown in linear and semi logarithmic plots in Fig. 6.

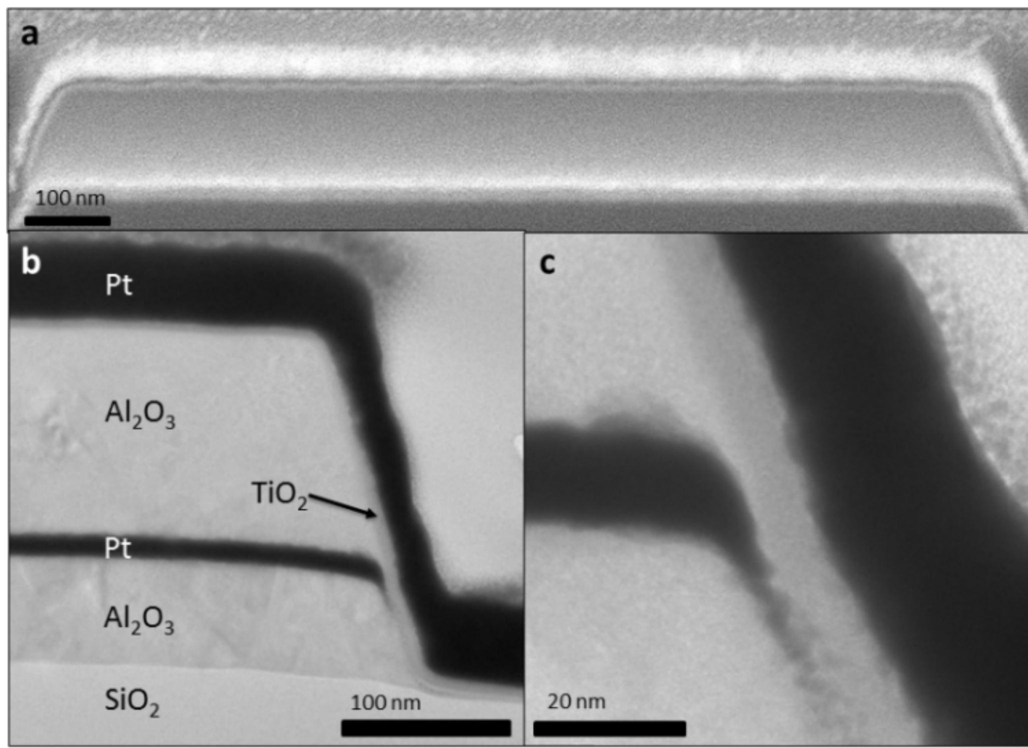

Figure 5: a) Cross-sectional SEM of a virgin 1μm device as shown by the dashed line from Fig. 4c, b) TEM of the material stack from one sidewall of a device, and c) higher magnification TEM of the Pt/TiO_2/Pt interface where memristive switching is expected to occur. Scale bars represent 100nm, 100nm, and 20nm, respectively.

3.3 Discussion

The cross-sectioned device revealed in the SEM and TEM shown in Fig. 5 closely resembles the intended device geometry illustrated in Fig. 4. Depositing 50nm Al_2O_3, 1nm Ti, 10nm Pt, and another 100nm Al_2O_3 resulted in bottom contact crossbar features approximately 160nm high with a slight gradient, ~20° from incident deposition angle, that is characteristic of thin films deposited by vacuum deposition through a small opening[67]. Al_2O_3 has a mean free path in vacuum of ~3m

at 1x10-6 torr vacuum[68], so we can assume all the material layers are deposited in direct line-of sight into 1µm-deep recesses into the resist. With recess depth approximately 5x the deposited feature height, it is understood that the deposited feature will have tapered vertical edges from resist pattern shadowing, and this benefits fabrication by allowing more conformal deposition of the top electrode metal onto the tapered vertical sidewalls. The Al_2O_3 above and below the bottom Pt electrode layer serve as dielectric barriers to ensure that; (1) current flows preferentially through the $Pt/TiO_2/Pt$ junction when the device is in the ON state and (2) sufficient electric field is applied to the $Pt/TiO_2/Pt$ when the device is in the OFF state. Masking the Pt bottom electrode with Al_2O_3 high dielectric barriers in the x-y plane limits the presence of conducting channels of the device to an exposed cross-sectional area of the tapered sidewalls defined by the two intersections of the top electrode and the bottom electrode in the z-y plane as defined in Fig. 4. The total cross-sectional area available for the formation of electrical current channels is then assumed to be approximately $10x1000nm^2$ on each side of the device, and this produces a total of $0.02\mu m^2$ active device area available for memristive switching, which is the same order of magnitude as smaller nano-fabricated devices. Switching at a compliance current as low as 5µA, as shown in Fig. 6, indicates this small active area for channel formation and current flow, which is comparable to previously fabricated $50x50nm^2$ devices using ALD-based switching layers with ~10µA operating current[32,69].

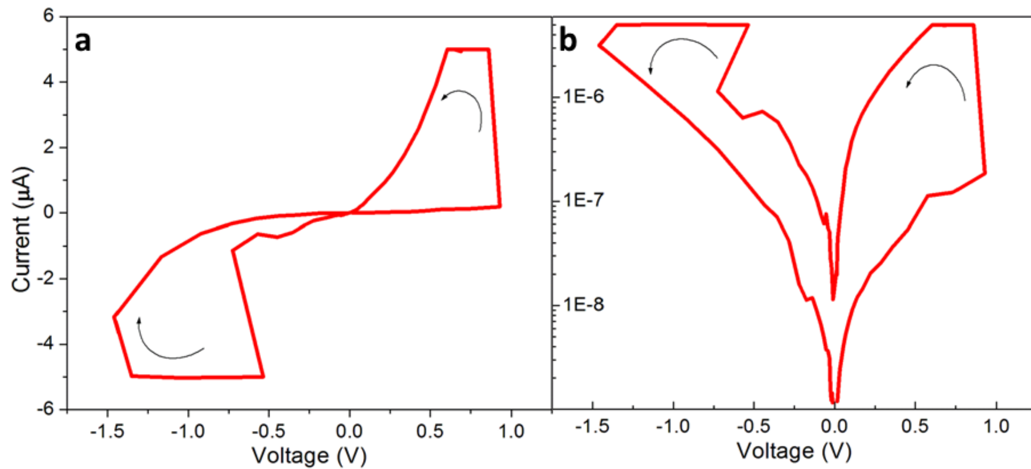

Figure 6: Current – Voltage measurements of memristive switching in a) linear and b) semi logarithmic curve plots.

Electrical current is expected to flow from the planar surface of the top Pt electrode as-deposited on the tapered wall feature through the 5nm TiO_2 layer into the cross-sectional edge of the Pt bottom electrode. The 2nm Ti deposited prior to 50nm Pt in the top electrode creates Ohmic contact on this side of the device, and the surface of the TiO_2 adjacent to the Pt bottom electrode edge creates Schottky contact. This Schottky barrier is the interface where switching is expected to occur when oxygen vacancies are supplied by drift[70]. The TiO_2/Ti interface creates a thin layer of sub-stoichiometric TiO_2 where oxygen vacancy concentration is high. This localized high concentration of positively charged oxygen vacancies carry charge and create conductive channels by drifting through TiO_2 when enough positive voltage is applied at the top contact. Channel formation therefore occurs most drastically through the TiO_2 layer interfacing with the vertical edge of the Pt bottom electrode. IV curve direction from Fig. 6a exhibits ON-switching with ~1V applied to the top

electrode. This polarity and low switching voltage confirm the switching mechanism of positively charged oxygen vacancies drifting from the interface between the 2nm Ti layer and the TiO_2 switching layer through the TiO_2 film rather than the adjacent Al_2O_3 dielectric barriers.

3.4 Conclusions

We have demonstrated that the well-studied physical switching mechanism of TiO_2 memristive devices can be implemented at the nanoscale without the use of costly or inconsistent nano-fabrication techniques such as e-beam lithography or nanoimprint lithography. Vertical RRAM devices with low operating current can be easily fabricated with current industrial technology. Much future work on the material system, fabrication processes, and device characterization is necessary to optimize electrical properties for robust endurance. However, the vertical RRAM device structure is a promising advancement towards commercial high-density low-current memristor technology.

Chapter 4

Corrosion barriers of silver telescope mirrors by plasma-enhanced atomic layer deposition

An urgent demand remains in astronomy for high-reflectivity silver mirrors that can withstand years of exposure in observatory environments. The University of California Observatories Astronomical Coatings Lab has undertaken development of protected silver coatings suitable for telescope mirrors that maintain high reflectivity at wavelengths from 340 nm through the mid-infrared spectrum. We present initial results of an investigation into whether plasma-enhanced atomic layer deposition (PEALD) can produce superior protective layers of transparent dielectrics.

Several novel coating recipes have been developed with ion-assisted electron beam deposition (IAEBD) of materials including yttrium fluoride, and oxides of yttrium, hafnium, and titanium. Samples of these mirror coatings were covered with conformal layers of aluminum oxide (AlOx) deposited by PEALD using trimethylaluminum as a metal precursor and oxygen as an oxidant gas activated by remote plasma. Samples of coating recipes with and without PEALD oxide undergo aggressive environmental testing, including high temperature/high humidity (HTHH), in which samples were exposed to an environment of 80% humidity at 80°C for ten days in a simple test set-up. HTHH testing show visible results suggesting that the

PEALD oxide offers enhanced robust protection against chemical corrosion and moisture from an accelerated aging environment. Mirror samples are further characterized by reflectivity/absorption and atomic force microscopy before and after deposition of oxide coatings. AlOx is suitable for many applications and has been the initial material choice for this study, although TiOx and HfOx were also studied. HTHH testing of this initial study resulted in unintentional condensation on all samples, which rendered the durability test quantitatively meaningless. However, proper methods for evaluating and comparing protected Ag mirror stacks of different barrier materials was established for successful work shown in Chapters 5 and 6.

4.2 Sample preparation

Initial samples were prepared on 2-inch diameter BK7 glass disks using the Physical Vapor Deposition (PVD) chamber at UCO (Phillips et al.[50]). The stacks are shown in Fig. 7. We proceeded with an optimistic approach that the ALD barrier layers would work well and that we should try several different variables (such as different underlayers and different ALD-produced oxides) in order to identify any combinations that stood out as either superior of inferior to the average.

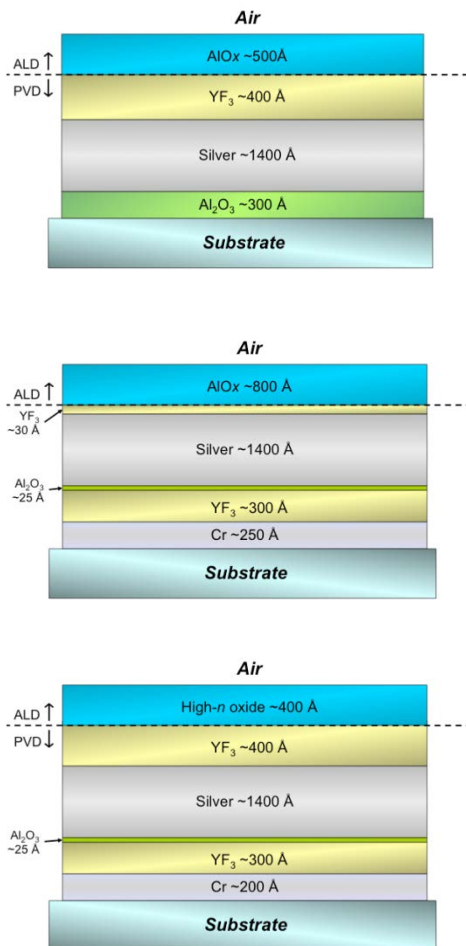

Figure 7: Schematics of the PVD samples prepared in the UCO coating chamber, with the eventual ALD oxide layer indicated. Properties to note: (a) sample has Al_2O_3 instead of Cr as a base layer; (b) sample has only a thin YF_3 layer against the Ag, to suppress oxidation during the ALD process; (c) general case with high-low index pair to boost reflectivity in the blue/UV (the high-n materials are AlOx, TiOx, and HfOx).

The samples fell broadly in two groups. The simplest (Fig. 7b) had only a very thin layer (30A) of YF_3 over the silver in order to protect the Ag from oxidation during the ALD process. This coating was designed to be purely protective of the Ag. The other group used a thicker (400A) layer of YF_3 (n~1.5) in combination with a

higher-index oxide (AlOx, HfOx, TiOx; $1.9<n<2.4$) in order to produce some enhancement of reflectivity in the blue (Fig. 7a, 7c). Such stacks will be required in practice for telescope mirrors, but their total thickness must be less than ~1000A or else emissivity in the thermal IR range can become objectionable.

The samples were measured for reflectivity on the UCO Varian-Cary 5000 spectrophotometer. The measured reflectivity fit model predictions closely. The samples were vacuum-packed until they could receive the final ALD top layer.

4.3 ALD process and analysis

Prior to ALD deposition, the PVD-produced mirrors were rinsed using organic solvents in a clean room environment. Oxide coatings were grown on the samples at 150°C using an Oxford FlexAl Atomic Layer Deposition System with a remote plasma attachment. Trimethylaluminum (TMA), Hafnium ethylmethylamide (TEMAH), and Titanium tetrachloride ($TiCl_4$) were used as the metallic precursors, and oxygen gas was the reactant source. Surface roughness of each sample was measured using atomic force microscopy (AFM) before and after the ALD layer, shown in Table 1.

Table 1: Surface roughness parameters before and after ALD oxide growth. Change in surface roughness is calculated as a percentage change from original surface measurements for Ra and Rmax. All roughness values are in nanometers.

Sample	underlayer	overlayer	initial R_a (R_{max})	final R_a (R_{max})	R_a % increase
A	30nm Al2O3	40nm YF_3 + 50nm AlOx	1.1 (7.5)	0.8 (6.4)	-27%
B	25nm Cr + 30nm YF_3	3nm YF_3 + 80nm AlOx	1.5 (9.1)	4.9 (25.5)	227%
C	25nm Cr + 30nm YF_3	40nm YF_3 + 50nm AlOx	1.1 (7.6)	14.9 (57.5)	1255%
D	25nm Cr + 30nm YF_3	40nm YF_3 + 40nm HfOx	0.8 (5.6)	1.0 (7.5)	25%
E	25nm Cr + 30nm YF_3	40nm YF_3 + 36nm TiOx	1.6 (11.9)	2.7 (13.9)	69%

Single line profile scans of 1µm were taken from an arbitrary spot on each mirror sample, and the initial roughness scans show some inherent deviation in the PVD coatings of the underlayers, silver films, and first overlayer material. Three of the five samples with identical material stacks (Cr/YF_3/Ag/YF_3) prior to ALD show some distribution in roughness, which suggests that the post-ALD roughness measurements also have unavoidable distribution from a true average. Therefore, we have assumed that the three samples with lower Ra % increase shown in Table 1

received conformal ALD coatings and thus are virtually unchanged in surface roughness.

Although ALD is credited with highly conformal growth properties, our measurements show drastic differences in surface roughness for some mirror samples. The samples with HfO_2 and TiO_2 overlayers showed insignificant change in surface roughness, however, the AlOx overlayers have various results. Surface roughness nearly doubled for the sample with the thickest AlOx overlayer. The most interesting observation comes from the two samples with identical overlayers and different underlayers. Both mirrors were put through the ALD process simultaneously for consistency, and one mirror showed virtually no change in surface roughness while the other experienced a surface roughness increase almost equal to the entire 50nm of deposited AlOx. The only sample with an AlOx underlayer rather than a chromium underlayer showed the expected conformal addition of deposited AlOx, but the second sample which included the typical Cr/YF_3 underlayer apparently experienced a columnar growth pattern on selective nucleation sites. This behavior is unlike any expected ALD growth pattern, and this study does not provide conclusive evidence to prove that the Cr/YF_3 underlayer is responsible for the increased surface roughness. However, it is clear that this surface roughness directly contributes to the decrease in reflectivity through light scattering, which is visible to the eye.

4.4 ALD process and analysis

The samples were measure for reflectivity; some curves are shown in Fig. 8. These values closely match the theoretical coating design, showing that the YF_3 layer was generally successful in preventing oxidation of the silver during the ALD process. This also shows that the optical properties of the ALD oxides are clearly sufficient to produce optically-excellent telescope mirrors. The one case where the reflectivity at $\lambda < 700$nm was a little below expected (by ~2% at 500nm and 10% at 350nm) was the case of Fig. 7b (or Sample B), where the thin oxidation-preventing layer was only 30A thick, suggesting that this layer should be somewhat thicker to prevent any noticeable oxidation during the ALD process.

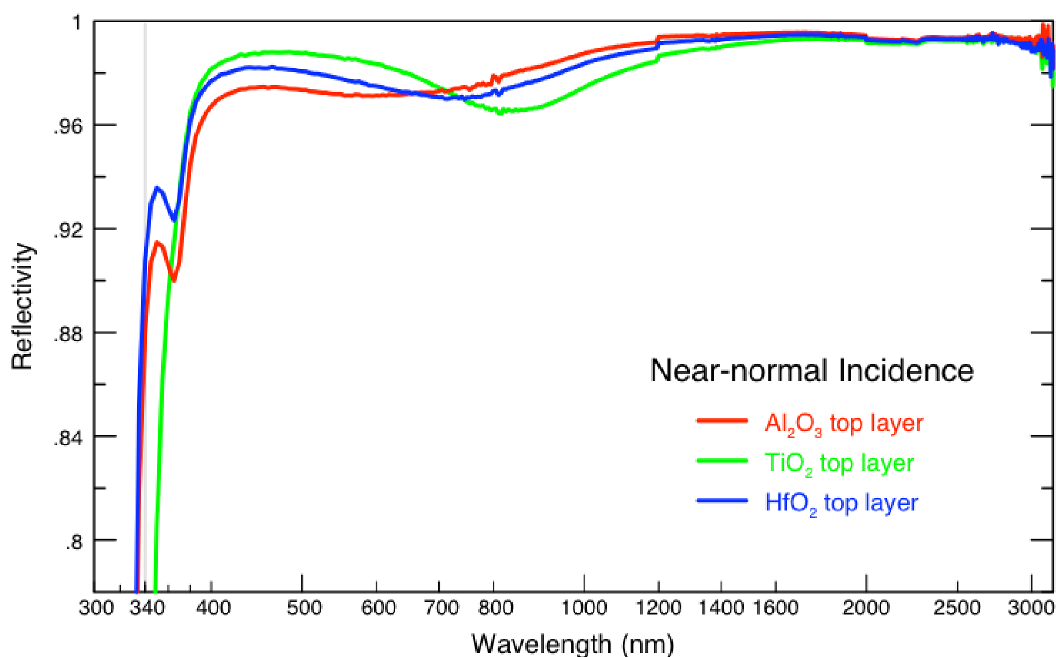

Figure 8: Measured reflectivity in the optical/NIR for three samples with top layers of AlOx, TiOx and HfOx. These are all excellent mirror coatings, with reflectivities very similar to theoretical design values. The curve for TiOx falls off in the UV due to absorption in the material; the fall-off in our sample is a little to the red of ideal, indicating slightly sub-stoichiometric composition.

The intended environmental test was to subject the samples to 80%-relative humidity at 80C for 10 days. We used the simple setup described in Phillips et al.[50] The samples were placed in a desiccator jar with wet KCl salt in the bottom to maintain relative humidity at ~75-80%, and the jar placed in an oven maintained at 80C. This tends to be a very aggressive test that usually shows some degree of degradation on the best of coatings, and we included some additional coated samples prepared by non-ALD means for comparison. Unfortunately, we have been plagued with condensation forming sporadically on the samples, and experience has shown

repeatedly that condensation on the coatings during the test leads to near-total failure. We believed we had learned how to prevent this condensation, but our test of these samples was again clearly affected with condensation. These samples were placed back-to-back in the holding fixture, and we found water between the samples when we separated them. Furthermore, the areas of corrosion on some samples followed the pattern of the condensed water joining them, suggesting a thermal coupling that lead to condensation on the outward-facing coated sides.

The effects of condensation in this environmental testing process must be seriously considered in evaluating endurance of mirror samples. However, in this preliminary phase of experimentation in which we attempt to find the most promising barrier material candidates, the corrosion mechanisms need to be isolated so that the protective effects of potential materials can bet better understood. Condensation was present on all of the tested samples, but fortunately, the mirror areas affected by condensation were easily identified, and exposed areas of the mirrors which were not affected by condensation showed more promising contrast between the different barrier layers. Fig. 9 shows the damaged areas affected by condensation and their respectful undamaged areas for the two most successful samples: the mirror with 80nm of AlOx and the mirror with 50nm of AlOx and no Cr underlayer. Identifying the success of some areas of these mirrors against the intended destructive mechanism of high temperature and high humidity without the unintended condensation gives us promising evidence that these ALD layers can prove to be effective barriers in a more precisely controlled environmental test.

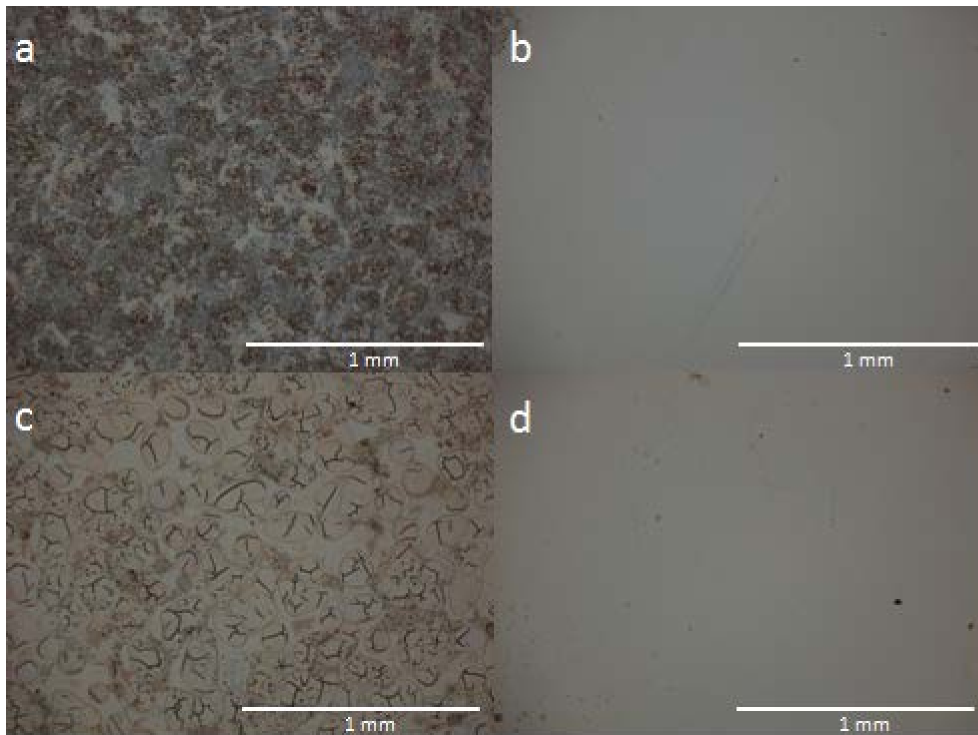

Figure 9: 2x2mm optical microscope images of (a) the 50nm AlOx-coated sample with no Cr underlayer corroded area affected by condensation and (b) the adjacent undamaged area and (c) the 80nm AlOx-coated sample corroded area affected by condensation and (d) the adjacent undamaged area.

While the environmental test was a clear failure, we were nevertheless able to learn a few things. In the case of the two partially undamaged (~20%) AlOx layered samples, the ALD-coated samples generally showed less or at least no more corrosion than their respective pure-PVD reference samples. The AlOx sample with the Cr underlayer, as well as those with TiOx and HfOx failed over their entire surfaces. Because the ALD growth temperature was held constant at 150°C for all three oxide barriers, the general failure of the TiOx and HfOx layers in the environmental testing

can possibly be attributed to a less dense, non-stoichiometric deposition, as these two materials conventionally have a higher temperature range for ALD growth. As expected, the control sample without the ALD oxide failed completely.

The small number of samples prevents us from drawing any definite conclusions. The fact that the two samples with relatively undamaged area were AlOx coatings suggests that HfOx and TiOx have no advantage over AlOx in terms of protecting the silver. There is also a suggestion (unsurprising) that thicker layers may confer more protection.

Chapter 5

Silicon Corrosion barriers for silver telescope mirrors: a comparative study of plasma-enhanced atomic layer deposition and reactive evaporation of aluminum oxide

Astronomical telescopes continue to demand high-endurance high-reflectivity silver (Ag) mirrors that can withstand years of exposure in earth-based observatory environments. We present promising results of improved Ag mirror robustness using plasma-enhanced atomic layer deposition (PEALD) of aluminum oxide (AlOx) as a top barrier layer. Transparent AlOx is suitable for many optical applications; therefore, it has been the initial material choice for this study. Two coating recipes developed with electron beam ion assisted deposition (e-beam IAD) of materials including yttrium fluoride, titanium nitride, and oxides of yttrium, tantalum, and silicon are used to provide variations in basic Ag mirror structures to compare the endurance of reactive e-beam IAD barriers with PEALD barriers. Samples undergo high temperature/high humidity environmental testing in a controlled environment of 80% humidity at 80°C for ten days. Environmental testing shows visible results

suggesting that the PEALD AlOx barrier offers robust protection against chemical corrosion and moisture permeation. Ag mirror structures were further characterized by reflectivity/absorption before and after deposition of AlOx barriers.

5.1 Introduction

While Ag thin films are routinely deposited in various applications, bare Ag quickly tarnishes due to reactions with oxygen and especially sulfur, and it corrodes easily via salt formation with halides. Thus, to provide long-lasting mirrors, Ag must be protected by barrier layers of transparent dielectrics in order to prevent tarnish and corrosion. The design of barrier layers has several constraints, and identifying suitable materials and deposition processes has proven challenging. Phillips et al.[48-50,71] discuss some details on the constraints and challenges and also report that certain materials, notably YF_3 in combination with high-index oxides, seem promising as barrier layers for Ag surfaces (i.e. barrier overlayers).

Telescope mirrors and barrier overlayers have traditionally been coated by physical vapor deposition (PVD). Barrie et al.[72,73] have demonstrated several successful recipes for protected Ag mirrors using various PVD techniques, and Jobst et al.[74] utilize similar deposition methods to deposit aluminum oxide and silicon dioxide as barrier layers for Ag mirrors. However, due to extrinsic factors such as the large areas of telescope mirrors, non-cleanroom environment during substrate

cleaning, and subsequent film deposition, pinholes are unavoidable and can significantly degrade coating lifetime by providing moisture and other chemicals a means to permeate through the mirror "stacks" (i.e., a structure made of a Ag mirror layer covered with barrier layers) and cause corrosion. Since PVD is assumed to be line-of-sight deposition, pinholes are exacerbated via self-shadowing. Atomic layer deposition (ALD), being conformal over complex three-dimensional structures, holds the promise of pinhole-free barrier layers. While ALD is a defined subset of chemical vapor deposition techniques, it is specifically advantageous for deposition processes requiring low temperatures, especially when the reactant gas is energized in a plasma, a process known as plasma enhanced ALD (PEALD). Furthermore, the low-stress, amorphous nature of ALD films is expected to improve overall mechanical durability as well by reducing or eliminating weak micro-crystalline grain boundaries. The excellent thickness uniformity achievable with ALD is another benefit.

5.2 Experimental Setup and Procedure

Briefly, mirror samples were prepared with most layers deposited by PVD in the University of California Observatory (UCO) coating chamber. The layers were produced either with direct electron beam deposition, or reactively with e-beam deposition under ion bombardment. The final top layer was added either with PVD or ALD to provide a direct comparison in performance. The two coating "recipes" are

shown in Figs 10 and 11. PVD deposition of all thin film layers except the top barrier layers were done simultaneously for samples A1 and A2 and again simultaneously in a another run for samples B1 and B2 to ensure that the only variable is the top layer. This allows an accurate comparison of the PVD vs ALD top-layer performance. The samples were characterized for reflectivity and then subjected to severe environmental stressing, roughly 10 days at 80C and 80% relative humidity.

Mirror samples A1 and A2 were prepared on 1x3-inch glass microscope slides, and samples B1 and B2 were prepared on 2-inch diameter BK7 glass disks. Most thin film layers, including Ag layers, were deposited by conventional e-beam evaporation in the custom PVD chamber. These depositions were done at room temperature and base pressure of ~10-6 Torr, and growth rate was calibrated using a quartz crystal microbalance within the chamber. All four samples contain a single 115nm Ag layer sandwiched by underlayers (i.e. layers formed between the substrate and Ag layer) and overlayers (i.e. layers formed on top of the Ag layer). The YF_3 layers in samples B1 and B2 were deposited using ion-assisted deposition (IAD) in an inert argon gas for densification and are designated in Fig 11 by (IAD) in the illustration. Ion assist is also used with ionized oxygen introduced to the chamber to deposit an oxide reactively. The overlayers were coated with a single AlOx top barrier layer deposited by either reactive e-beam IAD or PEALD. Samples A2 and B2 similarly received a top aluminum oxide layer with reactive e-beam IAD.

Samples A1 and B1 had their final layers deposited using PEALD. Prior to PEALD deposition, the PVD-produced mirrors were rinsed using organic solvents in

a clean room environment. Varying thicknesses of aluminum oxide (AlOx) were deposited using an Oxford FlexAl ALD tool. Trimethylaluminum (TMA) and oxygen gas ionized by inductively coupled plasma were used as aluminum and oxygen reactant sources, respectively. Substrate temperature and pressure were held at 150°C and 25mTorr, respectively, and plasma RF power was constant at 300W during oxygen gas ionization. Growth rate was calibrated using spectroscopic ellipsometry that provided both thickness and optical constants. During all sample preparation steps, vacuum was broken only to transfer samples from the custom PVD chamber to the PEALD chamber. The samples were measured for reflectivity on a Varian-Cary 5000 spectrophotometer to ensure that experimentally obtained spectrum for as-prepared specific mirror stacks closely match that of the ideally designed mirror stacks.

Samples A1 and A2 shown in Fig 10 demonstrate the initial direct comparison between reactive e-beam IAD and PEALD barrier layers. Both samples utilized e-beam deposition in the PVD chamber to deposit identical films on glass slides up to the 3nm AlOx layer. This coating recipe, along with all samples tested in this experiment, utilizes 22nm Y_2O_3 as a stripping layer on glass substrates to aid in the recoating process of mirror coating recipes applied to reusable optics[75]. The underlayer of 11nm TiN serves as the intermediate adhesion layer prior to Ag deposition due to the tested success of TiN as a base layer for smooth metal film deposition[76]. Non-reactive, non-IAD evaporated AlOx was chosen as the overlayer for the first recipe comparison and is designed to prevent oxidation of the Ag during

the subsequent reactive ALD or PVD deposition of the top AlOx layer. Previous work suggests that AlOx adheres well to Ag and also may offer the best adhesion surface for chemical vapor-based nucleation of the same material (Chapter 4). Subsequently sample A1 was removed from the PVD chamber and then loaded into the PEALD system where the sample was coated with 88nm AlOx (i.e. "88nm AlOx (ALD)"). Meanwhile, sample A2 remained in the PVD chamber and was coated with 82nm AlOx (i.e. "82nm AlOx (PVD)") by reactive e-beam IAD. The small difference in thickness (88 vs 82nm) is not believed to be important and is consistent within the different measurement abilities.

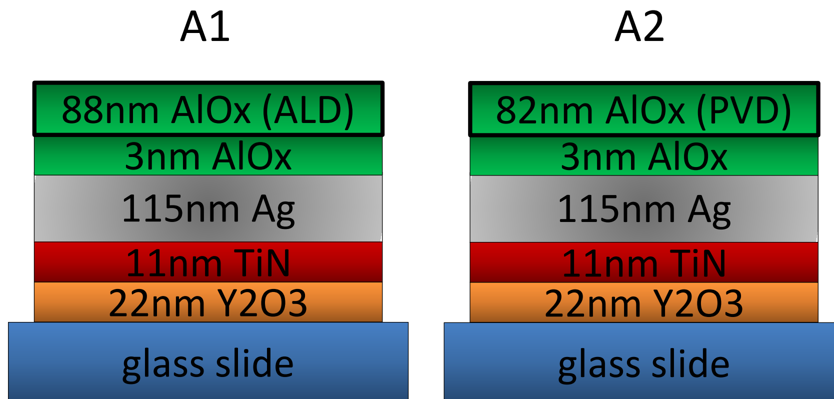

Figure 10: Schematic of samples A1 and A2 showing experimentally deposited layers. Note the 3nm anti-oxidation layer deposited from e-beamed Al2O3 which protects the Ag from oxygen ions during the reactive deposition of the ALD or PVD layer. Layer thicknesses not drawn to scale.

Samples B1 and B2 shown in Fig 11 were designed to directly compare 105nm AlOx barrier layers deposited by PEALD and reactive e-beam IAD with the

incorporation of unique overlayers designed to enhance UV/blue reflectivity. Both samples utilized e-beam evaporation to concurrently deposit multiple layers, as displayed in Fig 11, up to 36nm Ta2O5. The final AlOx barrier overlayer was deposited on sample B1 by ALD and on sample B2 by PVD, as before in samples A1 and A2.

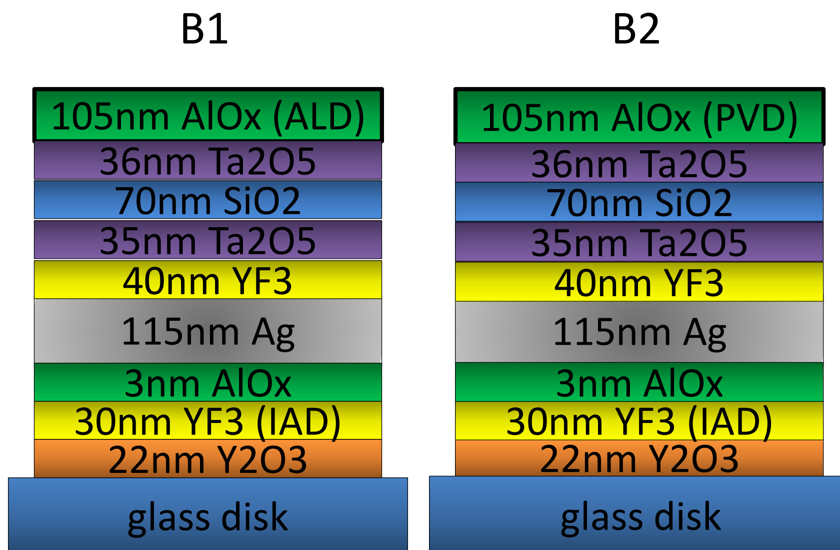

Figure 11: Schematic of samples B1 and B2 showing experimentally deposited layers. In this case, YF_3 acts as the anti-oxidation which protects the Ag. This stack has enhanced reflectivity in the blue/UV. Layer thicknesses not drawn to scale.

Prepared samples were subjected to environmental testing for 231 hours (~10 days) in an accelerated weathering environment described in Phillips et al.[50] The samples were placed in a desiccator jar with wet KCl salt in the bottom to maintain relative humidity at ~80%, and the jar was placed in an oven maintained at 80°C.

This aggressive environmental testing has been designed to push coating materials past failure and tends to yield at least some degree of degradation on even the best of coatings so that qualitative comparison can be made between these specific coating recipes. It should be noted that, in addition to the high temperature and humidity, there is an added component of salt ions in this environment. Samples are mounted vertically in the desiccator jar with only the bottom edge and corners in contact with the Delrin® mounting hardware in an effort to minimize potential condensation from contact with wet surfaces within the jar.

Post-stressing reflectivity measurements were made on "surviving" samples with enough remaining specular reflective surface area to fit within the spectrophotometer beam; any corroded regions lying in the spectrophotometer beam will scatter heavily and give a meaningless result. When a sample fails the environmental testing, it no longer functions as mirror to the eye, so it is not possible to obtain meaningful post-stressing reflectivity due to the beam of the Cary 5000 spectrophotometer, which is much larger than typical undamaged remaining area on a failed sample. However, the introduction of PEALD barrier layers has overcome the saturating over-aggressive effects of the environmental testing, and this study was able to include post-stressing reflectivity curves for samples with a significant enough portion of remaining undamaged Ag which fills the fixed reflectivity measurement spot size. The implications of this new dimension of coating recipe experimentation will allow for more quantitative analysis in future work with PEALD layers. Samples A1 and B1 coated with PEALD AlOx were partially corroded in the environmental

testing, however, the mirrors still functioned as specular reflectors to the naked eye, and so post-stressing reflectivity was measured. Fractional damaged areas of all four samples were estimated quantitatively using image processing software to identify corroded area ratios of each sample surface taken from side-by-side photography with uniform oblique lighting (Table 2).

5.3 Discussion

Reflectivity spectra are shown for all samples in Figs 12 and 13 with a logarithmic x-axis to emphasize visible/UV features. The resulting spectra reasonably match the reflectivity expected from coating models. In the case of the A1/A2 samples, this indicates the AlOx "anti-oxidation" overlayer was generally successful in preventing silver oxidation while transferring between chambers and during the ALD process.

Comparison between samples A1 and A2, with reflectivity curves shown in Fig 12, exhibits two spectra in reasonable agreement with the expected design reflectivity. The reflectivity model calculation does not account for absorption due to red-shifted surface plasmon resonance of metals with a changing dielectric function dependent on adjacent optical material[77], which is evident from the variation in reflectivity between ~350-400nm. Small increases in surface RMS roughness have

been shown to induce some scattering and slightly decrease reflectivity[77]. While calculated reflectivity does not account for surface roughness, we expect minor surface roughness (RMS ~1-2nm) for our mirror samples to explain the slight variation in reflectivity between simulated and experimental spectra. Sample A1 shows slightly higher reflectivity than A2 in the visible region. Since the only difference between samples A1 and A2 is the method of top barrier layer deposition, reactive e-beam IAD vs PEALD, this small difference in spectral response can be attributed to, for instance, the relative variation in film density of AlOx when comparing reactive e-beam IAD and PEALD. Alternatively, it may indicate that some O_2 ions penetrated the anti-oxidation barrier to produce some silver oxide in the PVD case of sample A2.

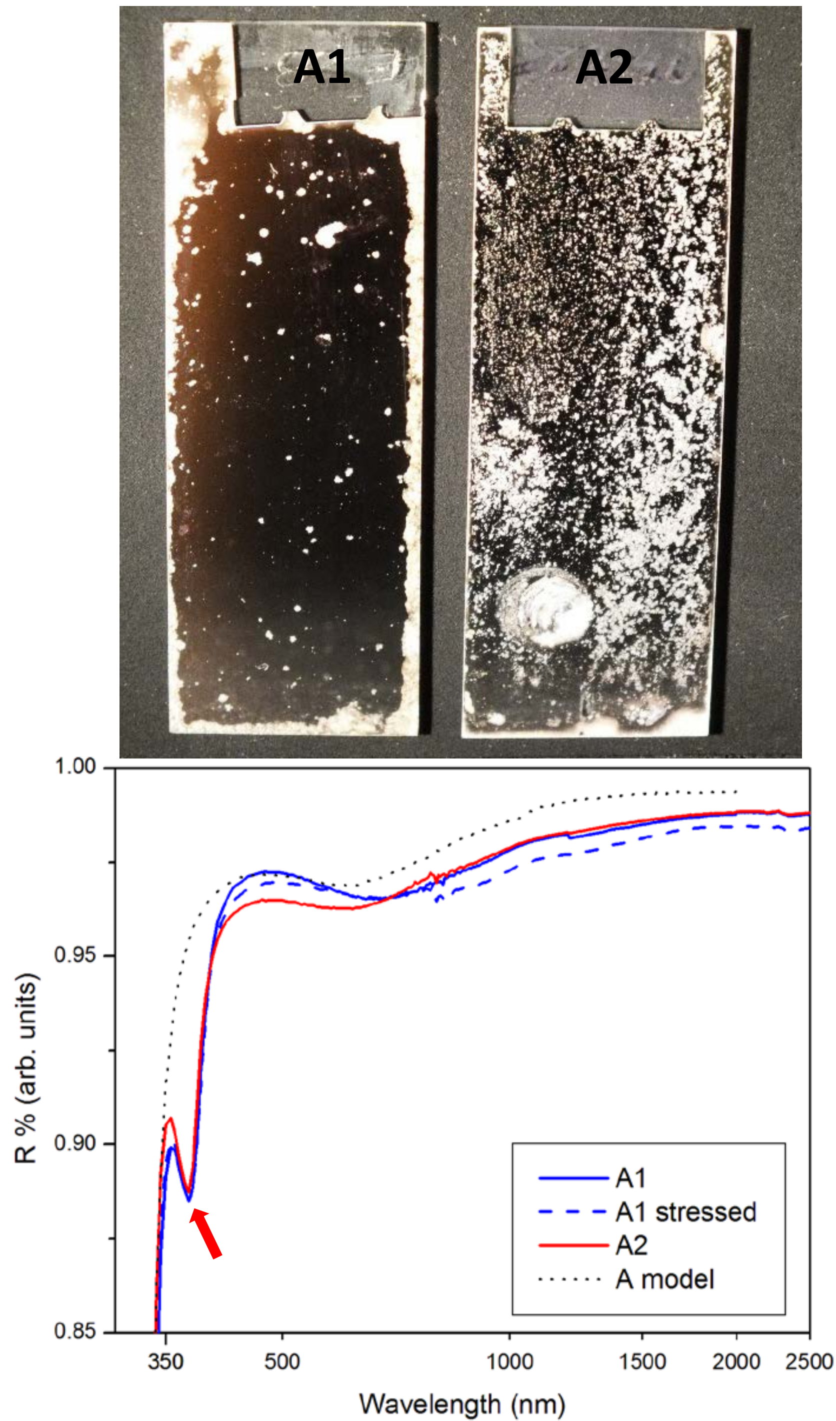

Figure 12: Top: photograph of samples A1 and A2 after 231 hours of environmental stress testing using a dark background and oblique lighting incident from the left, so dark areas indicate high specular reflectance while bright areas indicate scatter (corrosion). Bottom: Reflectivity is shown for A1 before and after the environmental

testing; post-stressing reflectivity could not be obtained from sample A2 due to lack of measurable undamaged areas. The model reflectivity of the coating design is shown for comparison. The absorption feature near 370nm (arrow) is caused by a surface plasmon resonance in the Ag; this feature is not predicted by the modeling software.

Samples B1 and B2 were designed to repeat the comparison between AlOx top layers deposited by PEALD and reactive e-beam IAD but with the application of a thicker overlayer stack to enhance UV/blue reflectivity. The 105nm AlOx barrier layer is also the thickest of all samples in this study, which likely also contributes to the superb endurance of sample B1. Fig 13 shows the reasonably matched reflectivity curves of samples B1 and B2 with both curves varying slightly from simulated spectra based on similar model assumptions noted for samples A1 and A2. The slight increase in visible reflectivity of sample B1 spectrum is attributed to the slightly lower optical density of PEALD-deposited AlOx as compared to the AlOx deposited by reactive e-beam IAD as previously mentioned discussing samples A1 and A2. Fig 13 clearly shows that the UV/blue spectrum-boosting constructive interference stack design reflects more light in the measured spectral range than samples A1 and A2, and the PEALD AlOx barrier layer does not seem to impede this design. Sample B1 also shows the strongest relative endurance after the environmental testing. This observation can be correlated with the conclusion that thicker overlayers are likely to provide better corrosion protection. Sample B1 shows significantly less surface damage than B2 post-stress testing, which is observable in Fig 13.

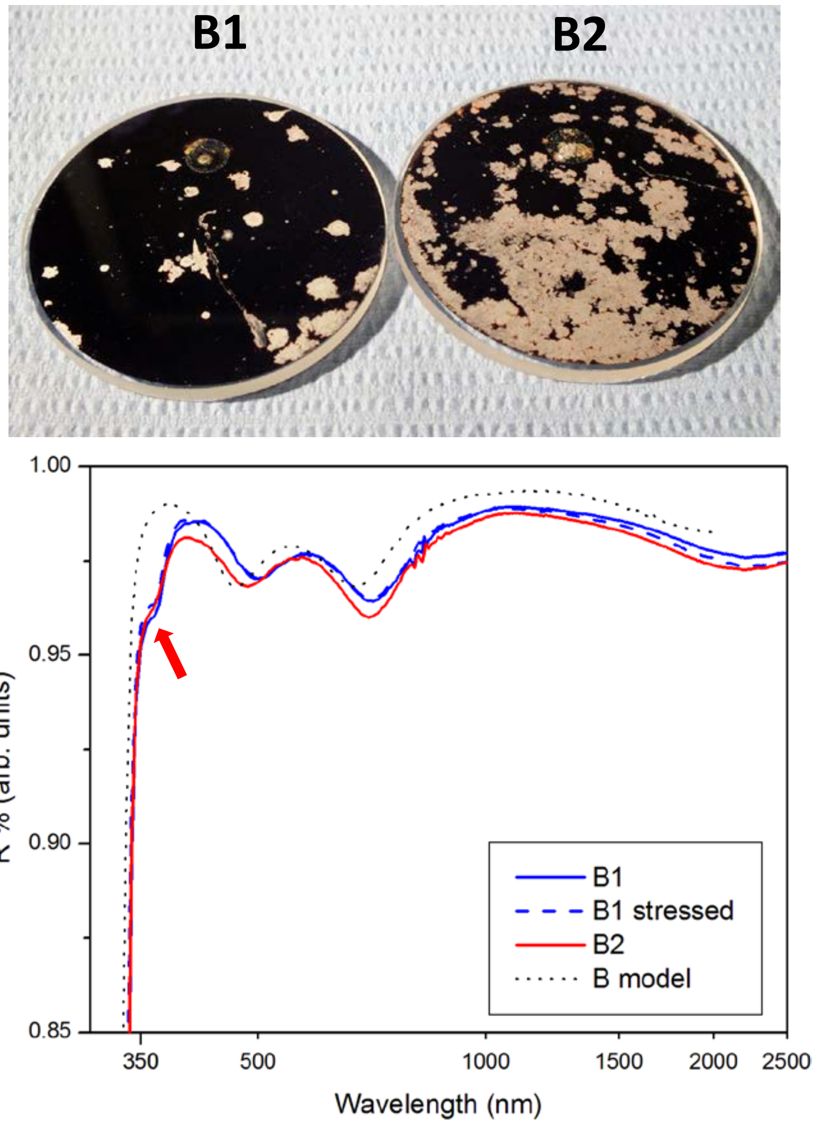

Figure 13: Same as Fig 12 but for samples B1 and B2.

Figs 12 and 13 show environmental stress testing results with significantly less damage to PEALD-based samples A1 and B1 when compared to their reactive e-beam IAD counterparts, A2 and B2. The damaged area ratios of each sample are quantified in Table 2. Samples A1 and B1 show significantly less damaged Ag area

and still yield specular reflection to the naked eye after environmental stress testing, and therefore reflectivity spectra were collected from these stressed samples. Partial corrosion of the barrier layers observed by the naked eye and reported in Figs 12 and 13 indicate that improvements should still be made to the mirror stack design to ensure greater long-term endurance of the barrier layers.

Visible results from Figs 12 and 13 indicate damage to the reflective Ag surface within the mirror coatings, but further work is necessary to analyze any microstructural damage inflicted on the AlOx barrier film and surrounding layers during environmental testing. While measuring film thicknesses with spectroscopic ellipsometry before environmental testing, the refractive index n of AlOx films grown by PEALD was found to be approximately 1.62 at 632nm, which is slightly less than the typical value of 1.65-1.7 in AlOx films deposited by PVD techniques. Variations in film density and the resulting change in spectral response have been observed in similar experiments of oxide deposition comparing chemical vapor-based deposition with various PVD methods[10,78,79,80]. Although higher film density may be intuitively desirable in corrosion barriers, resulting comparison between samples A1/A2 and B1/B2 shows that the slightly less dense films as deposited by PEALD create a more robust corrosion barrier. However, we attribute this enhanced robustness to the inherently conformal pinhole-free nature of the ALD monolayer growth process rather than the slightly lower film density. It is possible that the less dense AlOx films grown by PEALD sustain unseen damage such as increased porosity or hydrolyzed bonds[81,82] which may require more sophisticated analysis techniques to observe.

Schwinde et al.[82] observe the hydrolyzation of similar AlOx barriers on Ag mirrors after exposure to moisture by scanning electron microscopy of barrier cross sections.

Table 2: Fraction of damaged areas for samples A1 vs A2 and B1 vs B2.

Sample	**barrier layer**	**% damaged area**
A1	88nm AlOx (ALD)	14
A2	82nm AlOx (PVD)	38
B1	105nm AlOx (ALD)	12
B2	105nm AlOx (PVD)	54

The comparisons above were made to directly compare a single ALD vs PVD barrier layer with the remaining layers being identical. We have done several prior tests[71] where either the “stacks” varied slightly, or the coatings were produced on different coating runs, leading to the concern that some other parameter might be influencing the results (Chapter 5). However, in all of these tests, the ALD barrier layer samples consistently performed significantly better than the PVD counterparts, indicating the ALD barrier improved durability. The two tests reported in this work were designed to provide a direct comparison where only the top barrier layer differed, and thus they have the most relevance. Therefore, future work will include observations and more detailed analysis of various overlayer/underlayer materials

correlating physical properties to their effect on overall mirror recipe performance in environmental testing. However, based on our previous reported observations, samples not included in this work, and the direct comparison between top barrier layer deposition method in this study, we qualitatively conclude that PEALD-based AlOx barrier layers offer a general advantage over reactive e-beam IAD layers in the environmental testing of mirror coatings.

It should be noted that Schwinde et al.[82] included some ALD-AlOx samples in their study of protected-Ag coatings and reported no improvement in coating durability over PVD samples. The reason for this is unclear. It is possible their PVD process was "cleaner" and thus had fewer pinholes than our samples, which would implicate pinholes as the dominant cause leading to degradation. It is also possible that some other variables in the coating process were responsible for the different results. We note that their environmental stressing involved condensing water onto the surface of their samples, which may have accelerated hydrolyzation of the aluminum oxide. In any event, we have found consistently better performance with ALD-AlOx in multiple tests. We believe our cleaning and coating processes are typical for astronomical mirrors, and the environmental stressing with humid air is more representative of typical conditions for the mirrors, so our results may have more relevance to practical coatings for astronomical mirrors. However, the conflicting findings indicate more work is needed to fully understand all the parameters involved.

5.4 Conclusions

High-reflectivity silver mirrors with two corrosion barrier recipes have been fabricated using e-beam IAD and PEALD. Mirrors were environmentally stress tested in an accelerated environmental aging process using high temperature/high humidity conditions at 80°C and ~80% humidity for ~10 days. Reflectivity was measured pre- and post-stress testing, and visible surface damage was assessed in a comparison between deposition methods for top barrier layers of AlOx. Our pilot study of PEALD-based barriers has not yielded a perfect silver mirror coating, however, we have strong evidence that the ALD process does have promise as protection against tarnish and corrosion in addition to its inherently excellent optical properties. Environmental testing shows significantly higher endurance for mirrors coated with AlOx deposited by PEALD when compared with similar coatings deposited by reactive e-beam IAD. Further work on deposition process parameters and material layer selection will be integral to finding an optimized mirror coating recipe, and more precise control and analysis of environmental stressing and post-stress measurements will yield better understanding of the corrosion mechanisms observable on silver mirrors.

Chapter 6

Performance of silver mirrors protected with evaporated anti-oxidation layers and ALD aluminum oxide barrier overlayer

This work investigates different anti-oxidation materials deposited between silver (Ag) thin film mirrors and an aluminum oxide (AlOx) barrier overlayer and compares the effects on mirror durability to environmental stresses. Physical vapor deposition of various fluorides, oxides, and nitrides in combination with conformal layers of AlOx deposited by atomic layer deposition (ALD) are used to develop several novel coating recipes. Ag-AlOx samples with different anti-oxidation materials undergo aggressive high temperature (80°C) plus high humidity (80%) (HTHH) testing for ten days. Reflectivity of mirror samples is measured before and after HTHH testing, and image processing techniques are used to analyze the specular surface of the samples after HTHH testing. Most samples show better endurance after HTHH testing than samples with no anti-oxidation layer. Among the seven anti-oxidation materials used in this work, TiN, $MgAl_2O_4$, NiO, and Al_2O_3 anti-oxidation layers offer more robust protection against chemical corrosion and moisture when compared to samples with no

anti-oxidation layer. In addition, results show that the performance of the ALD-AlOx barrier overlayer depends significantly on the ALD growth process temperature. Because higher durability is observed in samples with less transparent TiN and NiO layers, we propose a figure of merit based on post-HTHH testing reflectivity change and specularly reflective mirror surface area remaining after HTHH testing in order to judge overall barrier performance.

6.1 Introduction

Large telescope optical components have traditionally been coated by physical vapor deposition (PVD). However, due to extrinsic factors such as the necessary large deposition area, non-cleanroom environment during substrate cleaning, and subsequent film deposition, pinholes are unavoidable and can be a significant endurance problem by providing moisture and other chemicals a means to permeate through the mirror stacks (i.e., a thin film mirror structure including adhesion underlayers, Ag, and barrier overlayers), leading to corrosion[83]. Since PVD conditions include line-of-sight deposition, pinholes are exacerbated via self-shadowing. The conformality of atomic layer deposition (ALD) over complex three-dimensional structures holds the promise of pinhole-free barrier overlayers[10]. The low-stress, amorphous nature of ALD films is expected to improve overall mechanical durability by reducing or eliminating weak crystalline grain boundaries. In addition, ALD provides excellent thickness uniformity as another benefit. However, ALD is partially incompatible with Ag since the chemically reactive

growth of an oxide material directly on Ag risks some partial oxidation of the Ag at the interface between Ag and the immediate oxide overlayer. Silver oxide is chemically unstable and partially absorbing in the UV/visible spectrum, which is significantly detrimental to mirror barrier adhesion and reflectivity[84].

In previous work (Chapter 5), a technique was developed to overcome this incompatibility between bare Ag and ALD depositing thin anti-oxidation ("anti-ox") layers using non-reactive e-beam evaporation directly after Ag film deposition. This technique has shown success in mirror durability tests, but the compatibility between various anti-ox materials and subsequent materials deposited by ALD has not been fully explored. In this reported work, eight mirror stacks were designed with different anti-ox materials, including no anti-ox material, under a common barrier overlayer, aluminum oxide (AlOx) deposited by ALD. AlOx was chosen as a common barrier overlayer for this experiment due to the previous success observed with AlOx deposited by ALD. In practice, it is highly-desired to keep substrate temperatures as low as possible during the coating process, both to reduce risk of damaging expensive substrate optics with thermal cycling, and especially to avoid damaging epoxy bonds in mounting hardware, which is becoming widely practiced. Therefore, we deposited the ALD-AlOx at both a common process temperature of 150°C for one set of eight samples and at a more practical temperature (for epoxy bonds) of 60°C for another set of eight samples. We report results of reflectivity, mirror durability, and correlations in mirror performance based on anti-ox material and barrier overlayer deposition temperature. Mirrors with anti-ox materials of TiN,

$MgAl_2O_4$, NiO, and Al_2O_3 appear more robust compared to mirror stacks with no anti-ox layer. However, mirror stack performance and overall desirability in observatory applications obviously depend on both reflectivity as well as mirror durability. Less transparent mirror stack materials, such as TiN and NiO as used in this work, may exhibit high durability but result in lower mirror stack overall reflectivity. In order to standardize and quantify the comparison of performance for mirror stacks in this work and future work, we propose a figure of merit to combine reflectivity and corrosion endurance test results.

6.2 Results and Discussion

Mirror coating recipes, illustrated in Figure 14, were deposited on 1x3 inch glass slides with a 22±1nm Y_2O_3 adhesion layer, 120±5nm Ag film, 5±1nm anti-ox layers, and 72±1nm AlOx barrier overlayer. The adhesion layer (Y_2O_3) and Ag film were identically deposited for all samples, followed by the deposition of one of the different anti-ox materials (YF_3, YbF_3, AlN, $MgAl_2O_4$, Al_2O_3, NiO, TiN, or no anti-ox layer). Ag was deposited at a rate of 4 nm/s while other materials were deposited at 0.5 nm/s or slower. In the case of nitride anti-ox layers (TiN, AlN), deposition was via reactive ion assisted electron beam deposition. In one case (NiO), the oxide was deposited by a slow evaporation of nickel metal in a background pressure of oxygen to reactively form the oxide; this oxide is most likely sub-stoichiometric. No ion-assist was used for the fluorides and other oxides, and the native material was e-beam

evaporated non-reactively. The samples were then exposed to air and transported to the ALD coating chamber in another location. All these samples were duplicated in order to be covered by a barrier overlayer of AlOx deposited at either 60°C or 150°C, leading to a total of 16 samples (8 anti-ox materials covered with ALD AlOx at two different deposition temperatures – Figure 14). The barrier overlayer of 72nm AlOx, common to all mirror samples with different anti-ox layers, was deposited by thermal ALD using trimethylaluminum and water for the Al and oxidizer, respectively.

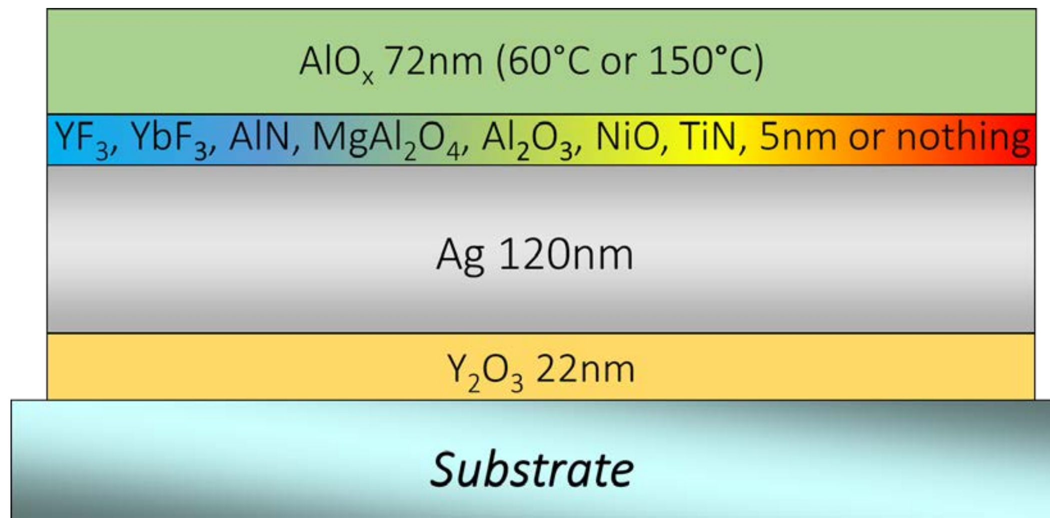

Figure 14. Illustration showing the protected mirror film stack with 8 different various 5±1nm anti-ox materials, including none, between the Ag film and AlOx barrier overlayer.

Specular reflectivity of all deposited mirror stacks was measured at a 7 degree incident angle from 200nm to 3µm using a Cary 5000 spectrophotometer prior to environmental stress testing. Spectroscopic ellipsometry and reflectometry measurements (SE) at 4 and 70 degrees over a 330-938 nm wavelength range were

taken using a FilmTek 2000 PAR-SE (Scientific Computing International, Carlsbad, CA) to calculate refractive indices of AlOx grown by ALD.

Mirrors were subjected to environmental testing for 231 hours (~10 days) in a high-temperature high-humidity (HTHH) accelerated weathering environment described in Phillips et al.[50] Briefly, the mirrors were placed in a desiccator jar with wet KCl salt in the bottom to maintain relative humidity at ~75-80%, and the jar was placed in an oven maintained at 80°C. Samples are mounted vertically in the desiccator jar with only the bottom end in contact with Delrin mounting hardware in an effort to minimize potential condensation from contact with wet surfaces within the jar. This aggressive environmental testing has been designed to push coating materials past failure and tends to yield at least some degree of degradation on even the best of coatings so that qualitative comparison can be made between these specific coating recipes. After HTHH testing, most of the mirror samples retained enough specular reflecting area to be re-measured with the ~0.5cm^2 spot size of the Cary 5000 spectrophotometer, except the four samples with YF_3 or YbF_3 as anti-ox layers. For these heavily corroded samples, remaining specular reflecting areas were too sparse and discontinuous to fit within the minimal Cary measurement spot size, presenting mainly diffuse reflectance and giving a meaningless result.

To evaluate the amount of remaining specular coating, HTHH-tested mirror samples were illuminated at an oblique angle by a halogen lamp from one side in order to highlight the diffuse scattering from damaged features in contrast to the black background reflected by the undamaged specular areas of the mirrors. Mirrors were

then individually photographed and analyzed using the color saturation technique in ImageJ [85] software to calculate the areal percentage of each mirror that remained undamaged (i.e. area primarily showing diffuse reflectivity).

6.2 Results and Discussion

The effectiveness of the anti-ox layers/AlOx corrosion barriers was studied by measuring the specular reflectivity of all samples before and after HTHH testing. Reflectivity of all 16 samples, graphed in Fig 15, shows the variation in mirror performance between stacks using 8 different anti-ox materials, including no anti-ox material. Reflectivity before HTHH testing is shown on top in Fig 15 a) and b), and post-HTHH testing reflectivity is shown on bottom in Fig 15 c) and d). The spectrum of interest is focused on the UV/visible range in order to emphasize features of the mirror stack reflectivity which are most sensitive to chemical change and corrosion. The 8 samples with AlOx deposited by ALD at 60°C are shown on the left in Fig 15 a) and c), and the 8 samples with AlOx deposited at 150°C are shown on the right in Fig 15 b) and d). All four frames of the figure share a common bare Ag reference curve (grey dot-dash line) to serve as a standardized guide to the eye which shows the optical effect of adding overlayers to a bare Ag mirror. All samples in this study show decreased reflectivity in the visible spectrum but constructive reflectivity boost around 350nm, which corresponds to the optical thickness of the ALD AlOx barrier overlayer. The samples with no anti-ox layer, represented with a black dashed line, can be interpreted as relative baselines for the reflectivity of Ag with only ALD AlOx barrier

overlayer. When the anti-ox layers are added, the reflectivity decreases (Fig 15 (a) and (b)). This decreased reflectivity prior to HTHH testing is attributed to absorption in the anti-ox layer. As such, TiN presents the highest absorption (lowest reflectivity) among all the samples under study. The samples with Al_2O_3 as an anti-ox layer present very low absorption, which can be attributed to the low refractive index and the low extinction coefficient of Al_2O_3[78]. While the less transparent anti-ox materials, TiN and NiO, show lower reflectivity before and after environmental testing, all samples except for YF_3 and YbF_3 endured the environmental stressing enough to be measured again after HTHH testing.

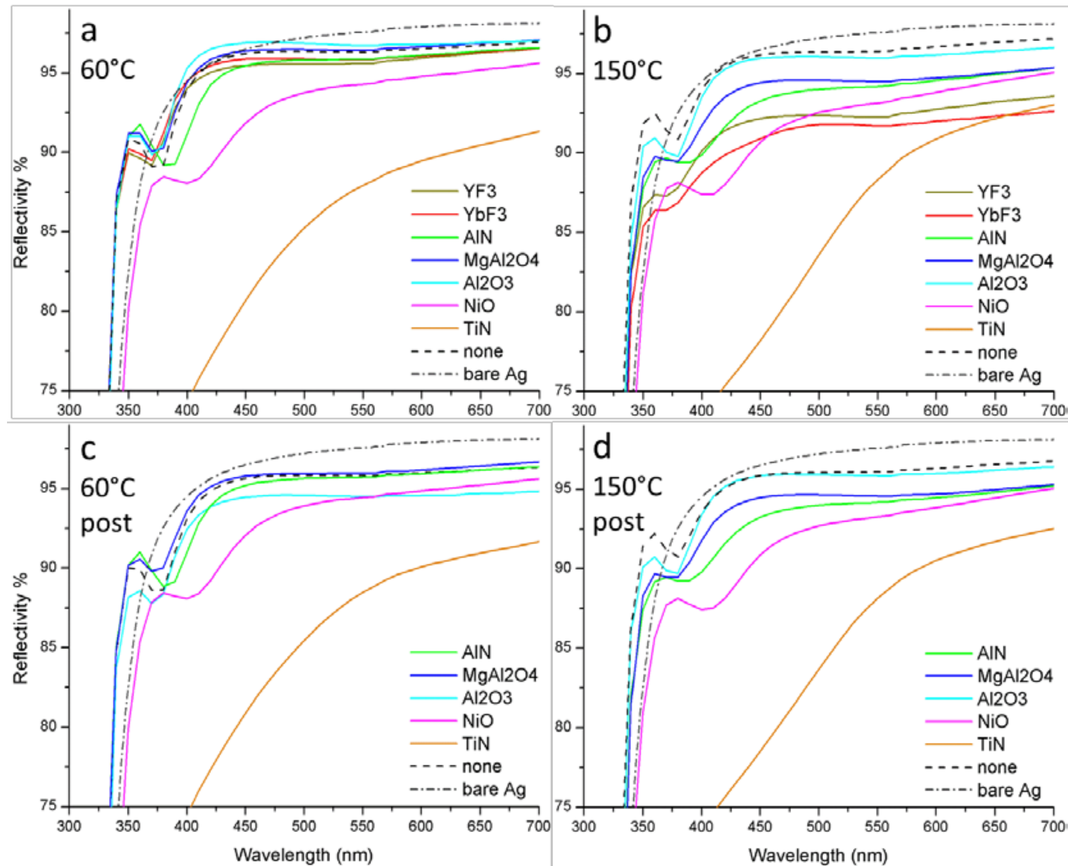

Figure 15: Reflectivity of 16 samples before (a, b) and after environmental stressing (c, d). Reflectivity was measured in areas undamaged by stressing. YF_3 and YbF_3 are not shown post-stressing as there were no undamaged areas. Left (a, c) show samples with AlOx deposited by ALD at 60°C, and right (b, d) show samples with AlOx deposited at 150°C. Bare Ag reference reflectivity (grey dash-dot) has been added to all four frames as a guide to the eye.

The samples with 60°C AlOx showed higher pre-HTHH testing reflectivity (Fig 15a) than their 150°C counterparts (Fig 15b). This increased reflectivity is attributed to lower refractive index due to decreased AlOx film density at 60°C[10]. Ellipsometry measurements of the calibrated 72nm AlOx layer grown at 60°C yielded a refractive index of 1.57 at 632nm, while films deposited at 150°C yielded a refractive index of

1.65 at 632nm. Reported values of amorphous aluminum oxide refractive index range from 1.5-1.7[10,78], which indicates that the 60°C AlOx film is significantly less dense, morphologically and optically, than that deposited at 150°C. While the 60°C samples showed higher pre-HTHH reflectivity, the 150°C AlOx-coated samples show less reflectivity loss than the respective 60°C samples after HTHH testing. We infer that a less dense barrier overlayer may have favorable optical properties but it is also more likely to degrade and become less transparent.

After assessing the specular reflectivity of the samples, the observable amount of specular-to-diffuse change in mirror area after HTHH testing was examined. Remaining specular reflectivity and areal damage, shown in Fig 16, can be qualitatively analyzed by eye with a common matte-black background as the reflected image from the photograph perspective. Damage from HTHH stress testing on mirror samples appears as non-black areas.

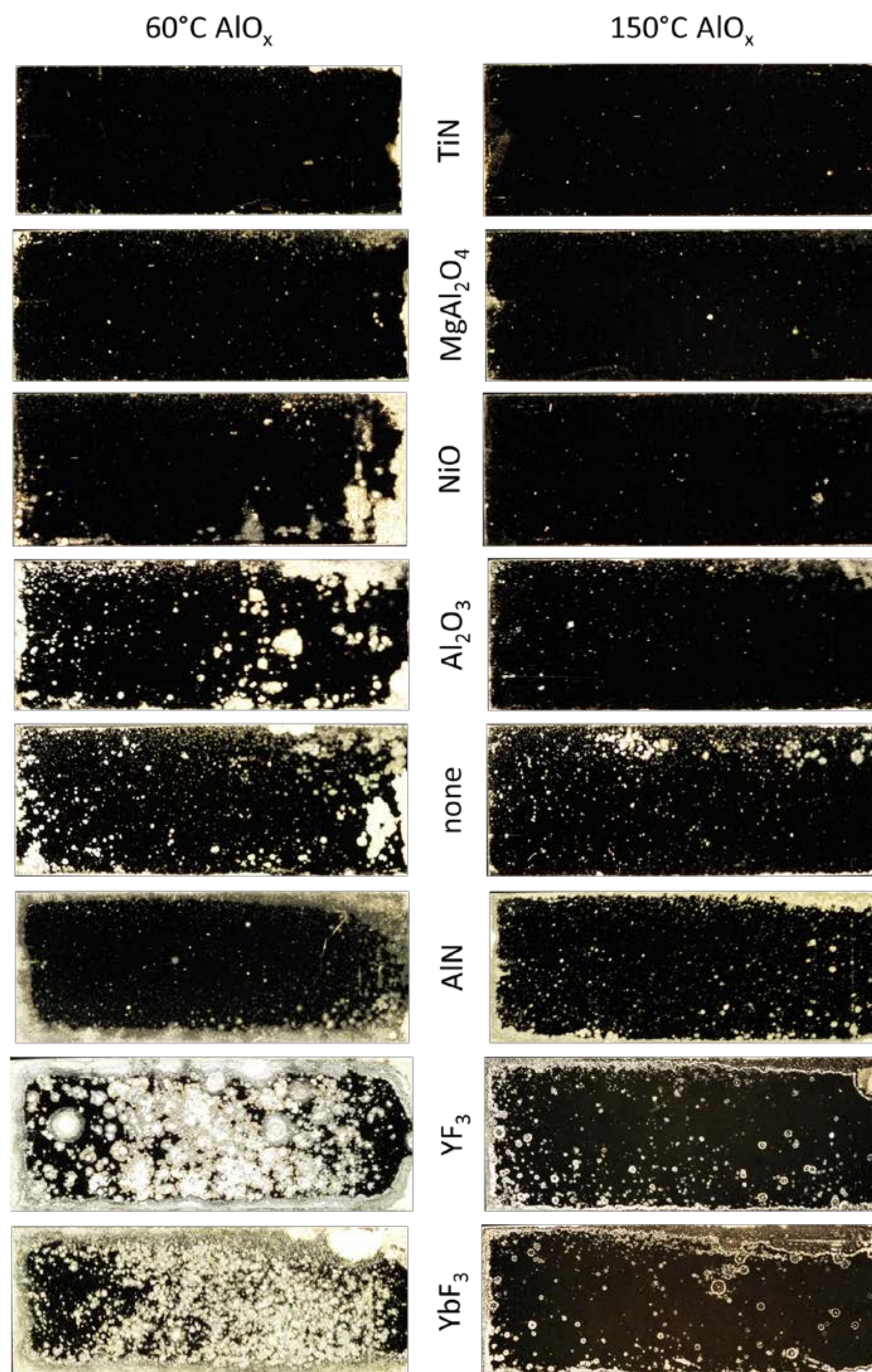

Figure 16: Pictures of the 16 protected mirror samples after ~10 hours of HTHH testing. Mirrors are photographed in a matte-black background to show specular reflection of undamaged mirror area as black. Other non-black colors and textures indicate diffuse reflection due to film damage during testing. Left side is 60°C AlOx; right is 150°C. The better corrosion resistance of the 150°C-deposited AlOx is obvious.

Mirror samples with AlOx grown at 150°C all show less damage than their counterparts coated with AlOx grown at 60°C. This uniform trend of less damaged 150°C AlOx-coated mirrors strongly suggests that mirror endurance performance is directly dependent on the morphological density of the barrier layer materials as inferred from refractive index measurements. Anti-ox materials exhibiting the best environmental stress endurance are TiN, $MgAl_2O_4$, NiO, and Al_2O_3. Mirrors without any anti-ox material performed relatively well, and samples with an AlN anti-ox layer underperformed those samples with no anti-ox layer. Although diffuse spots within the center of HTHH-tested samples give strong visual indication of barrier failure by eye, it must be noted that damaged area along sample edges contributes significantly to the areal calculation while not so apparent from observations by eye. The minor difference in performance between the AlN anti-ox samples and samples with no anti-ox layer demonstrate this comparison of edge vs. central areal damage; AlN anti-ox samples may appear more robust than samples with no anti-ox layer when comparing the mirror centers, but overall areal damage is still greater in the AlN anti-ox samples. YF_3 and YbF_3 anti-ox samples performed the worst and did not result in acceptable protected Ag mirrors. The failure of these fluorides is interesting because previous work has shown that thicker layers of the same materials seem to be effective barriers[50,71]. It is likely that the fluoride layers in this work are too thin to contribute with the same barrier mechanism as a thicker film and instead they create a less adhesive or less chemically stable film interface between the Ag and the ALD-grown AlOx layer.

Results of individual mirror sample analysis are quantified in Table 3. Mirror samples are ranked in descending order of durability which corresponds with the same descending order of qualitative pictures shown in Fig 16.

Table 3: Image analysis results of 16 HTHH-tested samples showing thickness of each anti-oxidation layer, % area still showing specular reflection, durability rank out of 16, and difference in % between samples with AlOx deposited at 60°C and 150°C.

anti-oxidation layer	**thickness (nm)**	**% specular area 60°C**	**rank 60°C**	**% specular area 150°C**	**rank 150°C**	**% change 150°C to 60°C**
TiN	4.0	92	4	94	1	-2
$MgAl_2O_4$	5.5	89	5	93	2	-4
NiO	4.0	78	8	92	3	-14
Al_2O_3	4.2	71	12	87	6	-16
none		67	13	84	7	-17
AlN	6.0	65	14	78	9	-13
YF_3	6.0	18	15	74	10	-57
YbF_3	6.0	15	16	72	11	-58

As seen in columns 3 and 5 from Table 3, all 150°C AlOx-coated mirror samples exhibited more remaining specular area than the 60°C samples with the same anti-ox layer. Although the variation in anti-ox layer thickness is minor, there is no

correlation between anti-ox layer thickness and damaged area, especially given that the mirror samples with no anti-ox layer show the median amount of damage. Differences in damaged area between 60°C and 150°C AlOx-coated samples loosely form three categories of performance in anti-ox material effectiveness; TiN and $MgAl_2O_4$ show the least difference in durability (2 to 4%), NiO, Al_2O_3, AlN, and no anti-ox layer show similar difference in durability (13 to 17%), and YF_3 and YbF_3 show the most drastic variation in durability between 60°C and 150°C AlOx-coated samples (57 to 58%). These three observable categories suggest that the protective role of the anti-ox layer, in relation to the protective role of the AlOx barrier overlayer, varies significantly with different anti-ox materials. Anti-ox materials that show the least amount of difference between 60°C and 150°C AlOx-coated samples exhibit the most durability with both 60°C and 150°C AlOx-coated samples (TiN and $MgAl_2O_4$). YF_3 and YbF_3, the anti-ox materials that show the greatest difference between 60°C and 150°C AlOx-coated samples, exhibit the worst durability with both 60°C and 150°C AlOx-coated samples. This trend emphasizes the importance of the anti-ox material directly adjacent to the Ag in overall mirror stack durability and suggests that the best anti-ox materials will unanimously show better durability than other anti-ox materials when combined with a variety of barrier overlayers deposited by ALD beyond AlOx.

Each anti-ox material's performance as a corrosion barrier can be attributed to characteristics of the material as well as its interaction with the adjacent Ag and AlOx films. Therefore, it is difficult to draw thorough conclusions that justify the mechanisms of success or failure of each material as an anti-ox layer. For instance, the

apparent high performance of TiN as an anti-ox layer may be attributed to possibly stronger chemical bonding between Ag and TiN, the intrinsic relatively high density and packing structure of TiN, or the possibly stronger adhesion and bonding between TiN and AlOx compared to other anti-ox materials in this study. Furthermore, the ALD chemical deposition process may more favorably nucleate AlOx in a dense, uniform film on TiN when compared to other anti-ox nucleating surfaces. However, the example of TiN as the most successful anti-ox material when measuring durability in the environmental stress test must be cross-referenced with the reflectivity spectra before selecting it as the most favorable anti-ox material in a protected Ag mirror stack. TiN is metallic and highly absorbing in the visible spectrum, and the reflectivity of both samples using TiN as an anti-ox material are significantly lower than all other samples with different anti-ox layers. Therefore, the results indicate, from the selection of materials in this work, that $MgAl_2O_4$ is the most favorable anti-ox material when designing protected Ag mirror stacks utilizing ALD-grown AlOx barrier overlayers. Both mirror samples utilizing $MgAl_2O_4$ as an anti-ox layer exhibit high reflectivity before and after environmental stressing. Durability of both $MgAl_2O_4$ samples are in the top tier of samples tested; the damaged area of both samples and the difference between damaged areas of the 60°C and 150°C AlOx-coated samples are just below those of the TiN samples. We speculate that success of $MgAl_2O_4$ as an anti-ox layer between Ag and AlOx may be attributed to the close match between twice the lattice constant of Ag and $MgAl_2O_4$. In fact, $MgAl_2O_4$, TiN and NiO were specifically selected for the close match in crystal structure and lattice constant with Ag (0.808nm [86],

0.424nm[87], 0.418nm[88] respectively, vs 0.409nm for Ag[89]). Lattice constant matching between Ag and the adjacent deposited film is hypothesized to contribute to adhesion between the film and Ag and therefore greater durability as a component of a protected Ag mirror stack. Mirror samples with $MgAl_2O_4$ may have also been successful due to the close matching chemical composition and possible miscibility with the AlOx barrier overlayer.

6.3 Figure of Merit

Judging overall mirror stack performance and desirability in observatory applications is complicated when evaluating raw reflectivity data and HTHH test performance, such as that Fig 15 and Fig 16, respectively. We propose a figure of merit (FOM) that can be used to judge quantitatively a mirror stack performance for practical application based on analysis of HTHH or similar environmental testing, combined with reflectivity measurements before and after such testing. This mirror figure of merit, which will be labeled M, can be defined by the product of the normalized quantities from the two fundamental metrics previously mentioned:

Equation 2

$$M = R_o * S$$

Equation 3

$$R_o = \int_{\lambda_1}^{\lambda_2} R d\lambda$$

Equation 4

$$S = \frac{A_S}{A_O}\frac{R_S}{R_O}$$

Initial reflectivity, R_o, is defined in Eq. (3) as the integral of the normalized reflectivity measurement within the desired spectrum defined by λ_1 and λ_2. Measurement of mirror change by environmental stress testing, S, is defined in Eq. (4) by multiplying the two components of measurable change due to environmental testing. The ratio of remaining specular reflective area and initial reflective area is defined as A_s/A_o. The ratio of integrated normalized reflectivity after environmental testing (measured on remaining specular mirror surface devoid of diffusely reflecting damaged area) and initial reflectivity R_o is the measurable change in specular reflectivity, defined as R_s/R_o. Convolution of the measurable change in specular reflectivity ratio with the first component of the FOM, R_o, cancels the FOM dependence on R_o, which results in the following simplified FOM:

Equation 5

$$M = R_S\frac{A_S}{A_O}$$

This proposed mirror performance FOM can be calculated by quantitative analysis of any type of corrosive environmental stress test and the resulting post-test reflectivity measurement. While the environmental testing factor of this FOM may be difficult to standardize within the scope of a large scientific community with numerous

different methods of testing barrier corrosive resistance and mirror durability, reflectivity measurements of specular mirror area can be quantitatively defined. Reflectivity as a normalized quantity, R_{norm}, can be defined to a specific spectral area of interest by integrating between specific wavelength boundaries of measurement as well as a specific range of magnitude in order to give more or less weight to specific spectral features within the FOM:

Equation 6

$$R_{norm} = \frac{1}{(\lambda_2 - \lambda_1) * (1 - R_{min})} \int_{\lambda_1}^{\lambda_2} [R - R_{min}] d\lambda$$

This equation for R_{norm} essentially draws a box around the spectral area of interest to be ranked with the FOM. Ag has inherent high reflectivity across the infrared spectrum beyond 1µm, and because most practical barrier coatings do not significantly affect reflectivity performance in this large spectrum, a FOM defined by such a large reflectivity spectrum will be less sensitive to the more pronounced changes in reflectivity in the UV/visible spectrum. Coating design requirements published by TMT define a benchmark minimum reflectivity in various spectra of interest for both the primary and secondary mirrors in order to achieve desired telescope performance. The TMT coating design requires a minimum of 80% reflectivity at 340nm, followed with a linearly increasing minimum requirement through the visible spectrum and a minimum required 97% reflectivity from 1500nm to 28µm[51]. We believe that these

TMT minimum mirror performance requirements are proficient metrics for defining a normalized FOM as follows:

Equation 7

$$R_{TMT} = \frac{1}{5.532}\int_{0.34}^{28}[R - 0.8]d\lambda(\mu m)$$

However, because of the previously mentioned desire to increase FOM sensitivity to more significant changes in UV/visible reflectivity rather than the relatively unchanging infrared spectrum, and due to common spectroscopic limitations of reflectivity measurement instrumentation, it is more practical to define λ_2 as a lower wavelength value below 28µm. The more practical and functional solution for applying various weights to spectra of interest with varying importance is to subdivide the total reflectivity spectrum into multiple normalized figures of merit. Continuing with the example of minimum reflectivity requirements defined by TMT, a more accurate FOM could be defined by the convolution of three normalized spectral regions of interest to better fit the specific coating design priorities:

Equation 8

$$R_{TMT} = R_{UV} * R_{vis} * R_{IR}$$

For example, R_{UV} can be defined as normalized reflectivity above the required 80% within the spectrum 340nm < λ < 400nm, R_{vis} above 90% within 400nm < λ <

1500nm, and R_{IR} above 97% within 1500nm < λ < 28μm. Other groups interested in highly reflective mirrors, including TMT, may develop more specific FOM definitions based on their needs, but the straightforward calculation of a reflectivity FOM can be better interpreted between different groups when integrating and normalizing according to defined values. Mirror coating performance FOM, *M*, and its constituent definitions of normalized reflectivity quantities are proposed as a template for further practical FOM development based on application-specific priorities. For example, mirror applications may require reflectivity weight at lower wavelengths in the UV spectrum, different weight of specific spectral bands depending on scientific interest, exclusion of weight in spectral bands such as atmospheric absorption bands, or weighted reflectivity integrated from semilog-plotted curves.

For mathematical simplicity in this first use of a mirror coating performance FOM, we have chosen to define R_{norm} from Eq. (6) with a baseline of 0.8 and within the spectrum of 340nm to 3μm; the Cary 5000 spectrophotometer used for reflectivity has a maximum observable spectrum measurement at 3μm wavelength. Using this specific spectral box of interest, R_{norm} has been calculated for the post-HTHH testing reflectivity measurements of all mirror samples from Table 3 and combined with their corresponding spectrally reflective area percentage and listed in Table 4 with a new ranking order of overall FOM performance.

Table 4: Figure of merit calculations for 16 HTHH-tested samples listed in the same descending order of HTHH test rank as Figure 16 and Table 3. R_{norm}, M, M rank, and difference in % between samples with AlOx deposited at 60°C and 150°C are listed.

anti-oxidation layer	**Rnorm 60°C**	**M 60°C**	**M rank 60°C**	**Rnorm 150°C**	**M 150°C**	**M rank 150°C**	**% change 150°C to 60°C**
TiN	0.776	0.714	7	0.788	0.740	6	-2.60
$MgAl_2O_4$	0.895	0.797	3	0.869	0.809	1	-1.17
NiO	0.884	0.689	8	0.870	0.800	2	-11.09
Al_2O_3	0.830	0.590	11	0.886	0.771	4	-18.15
none	0.881	0.590	10	0.903	0.758	5	-16.77
AlN	0.887	0.577	12	0.868	0.677	9	-10.07

Table 4 shows that the 150°C AlOx-coated mirror sample with $MgAl_2O_4$ anti-ox layer scores the highest with $M = 0.809$, which is in agreement with the previously mentioned qualitative assessment. While the two mirror samples with no anti-ox layer show high R_{norm} values, their lower ranking HTHH test results give both samples below average M ranks in overall performance. This observation further highlights the benefits of effective anti-oxidation layers in mirror stack durability. Both high-performing anti-ox materials, $MgAl_2O_4$ and TiN, show minimal difference in M between the 60°C and 150°C AlOx-coated samples (1.17% and 2.60%, respectively), which is similar to the observed difference in HTHH test performance observed in Table 3.

6.4 Conclusion

Several novel protected Ag mirror stack recipes have been demonstrated using PVD anti-oxidation layers of various fluorides, oxides, and nitrides in combination with conformal barrier overlayers of AlOx deposited by thermal ALD. Mirror stacks deposited using mixed PVD and ALD processes have yielded several robust mirrors with excellent optical quality. ALD deposition temperature and subsequent AlOx film density significantly affects the overall mirror stack durability, relatively independent of anti-ox material. However, the most durable samples with less damaged area show less dependence on AlOx top layer density than the less durable samples with more damaged area. Samples with TiN anti-ox layers exhibit the highest durability in environmental stress testing, but the small advantage in durability compared to the runner-up samples with $MgAl_2O_4$ anti-ox layers does not outweigh the significantly lower reflectivity due to the absorbing nature of TiN. $MgAl_2O_4$ is shown to be both robust and transparent as an anti-ox layer and is the most favorable anti-ox material used in this study. Development of a simple FOM ranking overall mirror stack performance provides quantitative analysis which supports the superior barrier properties of $MgAl_2O_4$/AlOx in this study. This new FOM will allow more standardized assessment of future work when optimizing PVD/ALD material combination mirror stacks in addition to other developing techniques for creating highly reflective robust mirrors.

Chapter 7

Silver film surface diffusion suppression by ion bombardment decreases surface plasmon resonance absorption

Silver thin films were deposited by electron beam evaporation for application as telescope mirrors using a custom PVD chamber from the University of California Observatories Astronomical Coatings Lab. Dielectric stacks utilizing silicon nitride and titanium dioxide are deposited by ion assisted electron beam evaporation onto Ag serving as protective barrier layers. Mirror stack blue spectrum reflectivity was improved by bombarding the silver (Ag) surface with argon ions in vacuum prior to deposition of subsequent dielectric stacks. We report the effects on bare Ag surface morphology and mirror stack reflectivity spectra caused by ion bombardment of the Ag and different holding-time in vacuum prior to ion bombardment. We suggest that surface diffusion of Ag and grain growth is suppressed by argon ion bombardment. Reflectivity of the mirror stack increases with a smoother Ag surface due to decreased surface plasmon resonance coupling.

7.1 Introduction

Silver-based mirrors suffer loss of reflectivity in at least some spectral region when Ag is coated with any protective film due to non-zero optical absorption of all materials. However, surface plasmon resonance (SPR) absorption is another source of loss of specular reflectivity in Ag films which is dependent on the dielectric function of material adjacent to the Ag. Although the Ag SPR absorption phenomenon is widely utilized in SERS detection applications utilizing nanostructured Ag and Ag nanoparticles[90], the coupling of incident light with the SPR mode of ideal smooth Ag films is much less efficient (and therefore allows greater reflectivity) due to the lack of Ag nanostructures and sharp features. However, if Ag thin films roughen by forming larger nanostructured morphologies with sharper edges and more distinct surface features, coupling efficiency between incident light and Ag SPR increases absorption, which results in lower reflectivity of the Ag thin film in the UV/visible spectral region[91,92]. Subsequent deposition of dielectric overlayers onto rough Ag surfaces results in red shifting and significant increase of SPR absorption amplitude, which is also directly dependent on the amplitude of the adjacent overlayer dielectric function[93]. While many users and producers of Ag thin films, including Thirty Meter Telescope (TMT) coating guidelines, recognize the undesired SPR absorption due to formation of large Ag grain formation and rougher Ag surfaces[51], the Ag deposition parameters during film formation, specifically pressure, temperature, and deposition rate, are identified as the controlling factors of Ag thin film morphology[94,95,96]. Argon ion bombardment of post-deposited Ag is often applied as a surface decontaminating and cleaning technique in order to improve surface free energy prior to a subsequent

material coating ex-situ Ag deposition, such as SERS detection applications[97,98]. Effects on surface morphology after post-deposition Ar+ ion bombardment have been studied for single crystal and polycrystalline Ag films[99,100], and optical properties of Ag films have been studied in-situ during Ar+ ion bombardment of the Ag surface[101]. However, to the best of the authors' knowledge at time of publication, post-deposition Ar+ ion bombardment has not been discussed in the application of improving optical properties of protected Ag or decreasing SPR absorption.

In this work, we observe that 120nm Ag thin films deposited by e-beam evaporation experience surface diffusion and grain growth in vacuum at room temperature immediately following deposition. Resulting Ag films therefore exhibit rougher surfaces and larger grains prior to protective dielectric layer deposition. Measured reflectivity of protected mirror stacks with dielectric materials on Ag films with larger grains show reflectivity loss as a result of SPR absorption coupling with larger Ag grains. We also report for the first time, to the best of the authors' knowledge, Ag mirror reflectivity is improved by exposing Ag thin films to argon ion (Ar+) bombardment in vacuum immediately after deposition prior to being coated with protective dielectric overlayers. Reflectivity performance of Ag surfaces with/without Ar+ exposure are correlated with scanning electron microscopy (SEM) and atomic force microscopy (AFM) characterization of the respective thin film surfaces in order to analyze the possible effects of Ar+ exposure on Ag surface morphology and resulting reflectivity.

7.2 Sample Preparation and Experimental Details

Bare Ag mirrors were deposited by e-beam evaporation without protective dielectric layers in order to observe morphological features of bare Ag films with and without Ar+ ion exposure. An adhesion layer of 22nm Y_2O_3 was first deposited on chemically cleaned microscope slides using ion-assisted deposition (IAD). Ag was then evaporated at a rate of 4nm/sec to form an opaque film with 120nm thickness. After the Ag target cooled for ~5 minutes in vacuum, one of the Ag film surfaces was exposed to Ar+ ion bombardment for 45 seconds. A second control Ag thin film sample was not exposed to any ion bombardment. Contrasting bare Ag films were analyzed using SEM (FEI Quanta 3D Dualbeam) and AFM (Ambios Q-Scope) to observe Ag grain size and roughness.

Two full mirror stack (adhesion underlayers, Ag film, and barrier overlayers) samples were deposited identically with the exception of post-Ag treatment in order to observe the effect of different Ag film surface morphologies interacting with dielectric barrier overlayers measured by reflectivity. Similar to the first two samples, Ag films were deposited identically on adhesion layers of 22nm Y_2O_3, 30nm YF_3, and 2.5nm Al_2O_3 on microscope slides. After Ag deposition, the bare Ag surface of one sample was exposed to Ar+ ion bombardment for 45 seconds while the control sample did not experience any ion exposure. Both samples were subsequently coated with the remaining identical top barrier layer combination of 30nm Si_3N_4 (using IAD) and 16nm TiO_2 which is designed to boost reflectivity in UV/visible spectrum. Reflectivity for

these mirror stack samples, as well as all subsequent mirror samples, was measured using a Cary 5000 Spectrophotometer at 7 degrees incident angle from 200nm to 3µm.

A final experiment was designed to observe the effect of Ar+ ion exposure on four Ag mirror stacks while varying the idle time in vacuum of the bare Ag films after ending Ag deposition and before Ar+ ion exposure. These four mirror stacks were designed and deposited with 22nm Y_2O_3 (using IAD) as an adhesion layer on glass, followed by 120nm Ag. After Ag film deposition for all four samples, three of the samples were exposed to 45 seconds of Ar+ ion bombardment after different amounts of idle time sitting in vacuum (90, 375, and 680 seconds), and one control sample was not exposed to any ions. Identical barrier overlayers of 30nm Si_3N_4 (using IAD) and 16nm TiO_2 were subsequently deposited on all four samples. Si_3N_4 deposition began 1140±60 seconds after the end of Ag deposition for all four samples. Reflectivity of the four samples was measured. Absorption features due to SPR coupling were fit to Gaussian functions and analyzed mathematically.

7.3 Results and Discussion

AFM measurements of the two bare Ag film samples, shown in Fig 17, confirm the contrast in film morphology and roughness between that of as-deposited Ag with no ion exposure and Ag exposed to Ar+ ions. As-deposited Ag rms roughness over a 10µm area scan is measured to be 2.82nm, shown in Fig 17a on the left, while Ag exposed to Ar+ ions has a lower measured roughness over the same 10µm area of

1.473nm, shown in Fig 17b on the right. As-deposited Ag exhibits a rougher surface than Ag exposed to Ar+ ions with features larger in both x-y and z dimensions. Although these more distinct z-dimensional features on the as-deposited Ag surface appear random without any periodicity, the high density of sharp edges is expected to provide coupling sites of increased SPR absorption and scattering when an adjacent dielectric film is deposited.

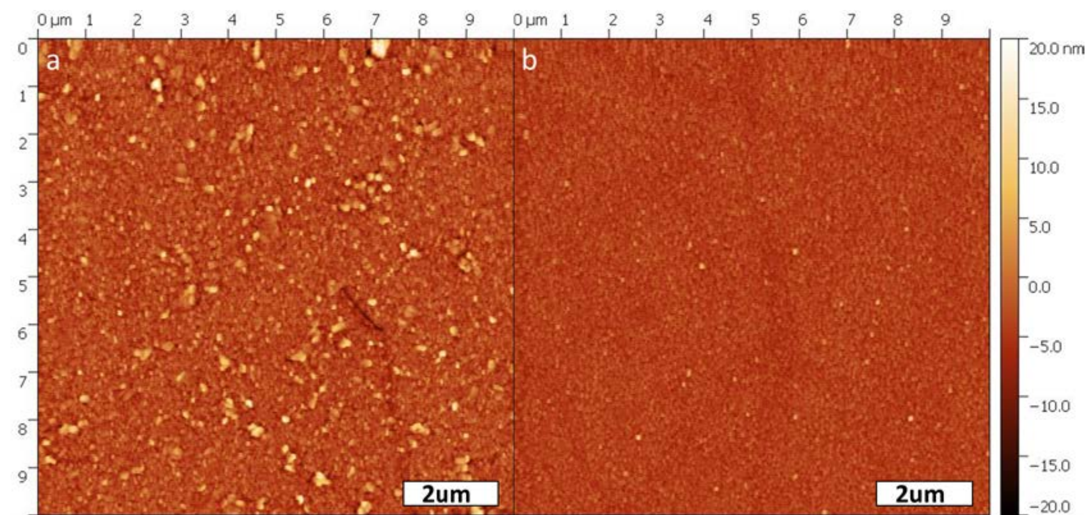

Figure 17. 10µm area AFM scans of a) as-deposited Ag surface and b) Ag surface after 45 seconds of Ar+ exposure.

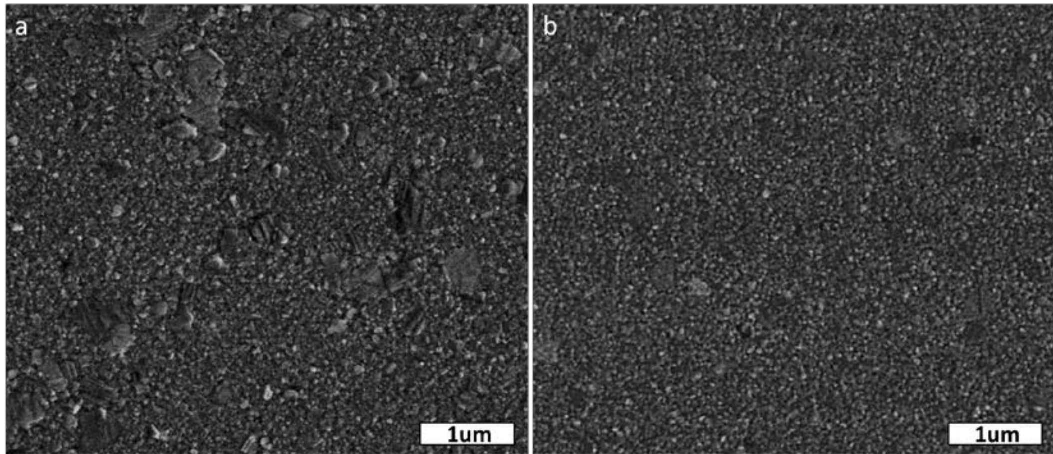

Figure 18: SEM images of a) as-deposited Ag surface and b) Ag surface after 45 seconds of Ar+ ion exposure.

Higher contrast x-y surface features between Ag samples deposited with and without Ar+ ion bombardment are observed by SEM as shown in Fig 18. The as-deposited Ag film, shown in Fig 18a on the left, exhibits a wider distribution of grain size and features when compared to the Ar+ ion bombarded Ag film shown in Fig 18b on the right. In both Ag films, a “background” of grain sizes ~<50nm is observable. However, as-deposited Ag without ion exposure shows some larger grains sizes ~>200nm which can be assumed to be higher aspect ratio grains that are significantly wider than the Ag film thickness of 120nm. Such high-aspect ratio Ag grains are not expected to form in aligned parallel plane with the Ag thin film, and therefore, high-profile sharp edges exist at the boundaries of these larger grains observable in Fig 18a. Note that the magnification of Fig 18 SEM images is nearly double that of the AFM scans in Fig 17 in order to better highlight the larger grain edge features.

Comparing surface morphologies of the two bare Ag films indicates that 120nm Ag deposited by e-beam evaporation forms an inherently rough surface with a wider distribution of larger grain sizes within the film. Exposure of the Ag film surface to Ar+ ion bombardment in vacuum somehow alters the Ag surface. However, the possible mechanism of Ar+ ions affecting Ag grains cannot be comprehensively understood with SEM and AFM observations alone.

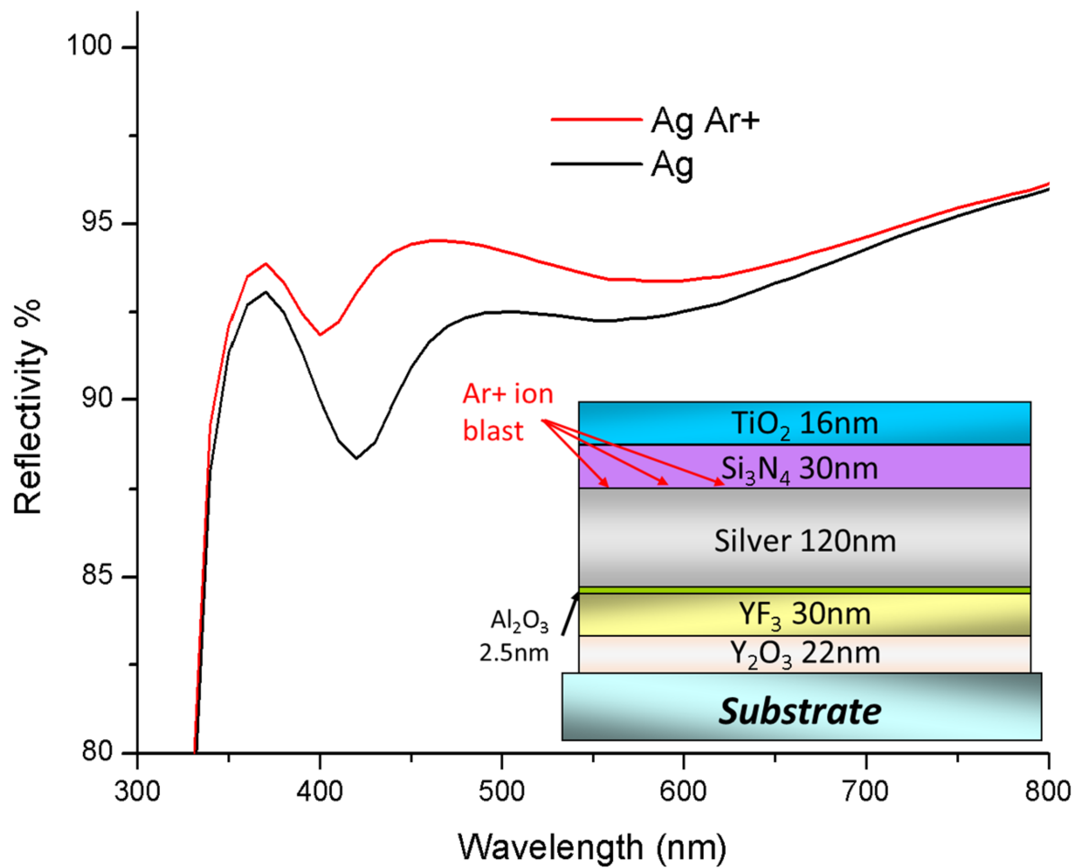

Figure 19: Reflectivity of as-deposited Ag and Ag exposed to Ar+ ion bombardment plotted with emphasis on the UV/visible spectrum features. The illustrated mirror stack, with red arrows indicating the bare Ag surface which was exposed to Ar+ ions in vacuum, is inset.

Improvements to mirror reflectivity after Ar+ ion exposure to the Ag film surface are shown in Fig 19. The reflectivity intensity in the $330<\lambda<800$nm spectrum is higher for the Ar+ ion bombarded sample than the as-deposited Ag film control sample, notably ~3-4% higher in the blue spectrum. Besides intensity gain, relative shift in the reflectivity curve features are also noteworthy. The local minimum feature at ~420nm, which can be attributed to the combination of Ag bulk plasma absorption, Ag SPR absorption, TiO_2 constructive interference, and Si_3N_4 constructive interference, is blue-shifted to ~400nm for the Ar+ ion bombarded sample.

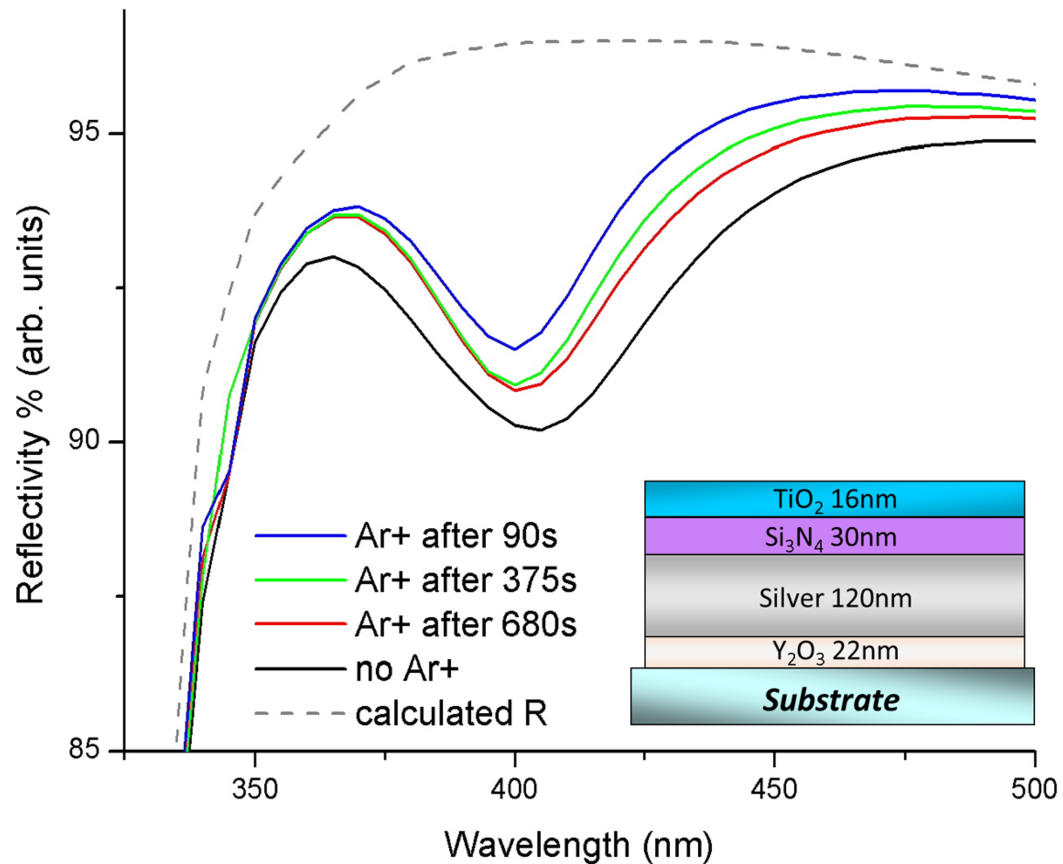

Figure 20: Protected mirror thin film stack illustration (bottom right) and resulting reflectivity spectra of 4 samples with 45 seconds of Ar+ exposure after waiting (blue) 90 seconds, (green) 375 seconds, (red) 680 seconds after Ag film deposition, and no Ar+ ion exposure (black). Si_3N_4 was deposited 1140±60 seconds after Ag film deposition for all 4 samples. Calculated reflectivity of the mirror stack is plotted with a grey dashed line.

To better understand the possible mechanism of Ag film smoothing by Ar+ ion bombardment, an experiment was designed to control idle time of the bare Ag films in vacuum and measure corresponding changes in reflectivity. Four final Ag mirror samples were designed and deposited using identical deposition parameters as prior samples with the exception of idle time between the end of Ag film deposition and a 45 second exposure to Ar+ ions. Resulting reflectivity of the four samples are

shown in Fig 20, and the mirror sample stack is illustrated in the inset on the right. A clear trend can be observed between mirror sample reflectivity intensity and idle time between Ag deposition and Ar+ ion exposure. As idle time in vacuum between Ag deposition end and Ar+ ion exposure decreases, reflectivity intensity increases across the UV/visible spectrum. The mirror sample which was exposed to Ar+ ion bombardment only 90 seconds after Ag deposition has the highest performing reflectivity, while the control sample which was not directly exposed to ions has the lowest reflectivity in the set of four samples. The trend observable in Fig 20 confirms that Ag morphology change is directly affected by Ar+ ion exposure.

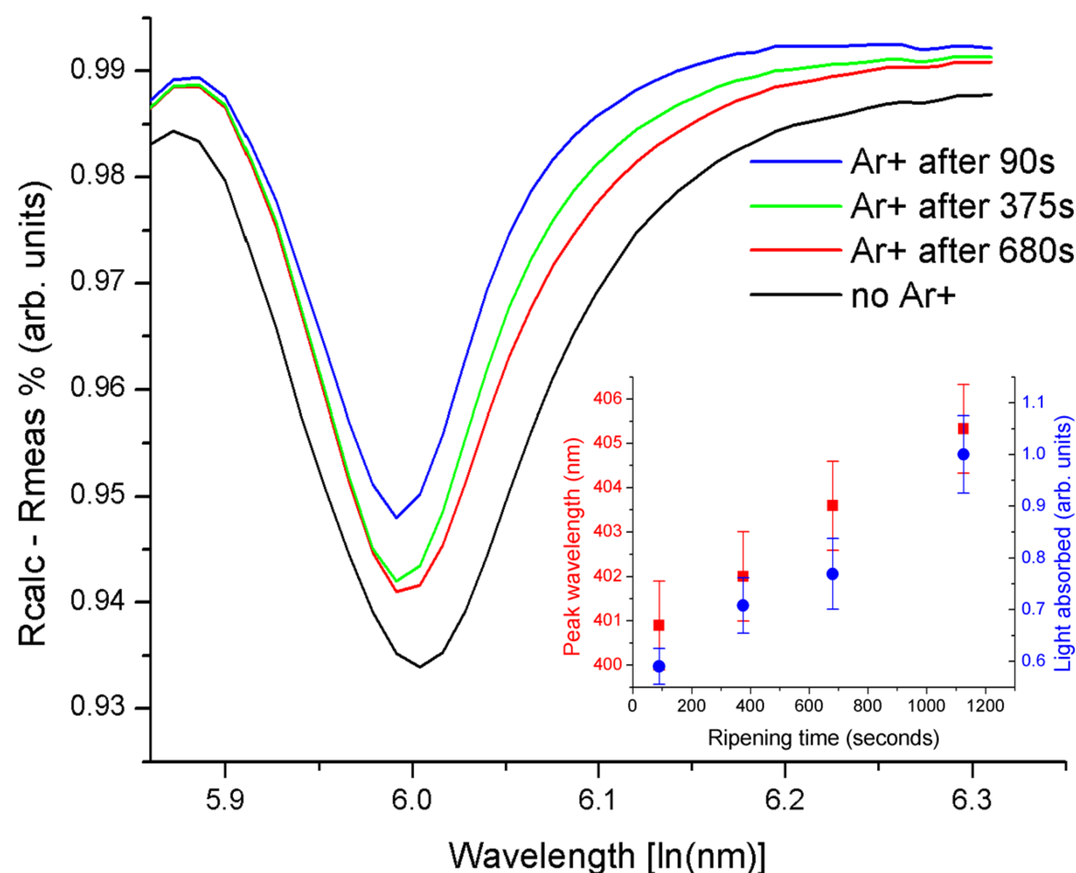

Figure 21: Measured reflectivity curves are subtracted from the baseline calculated reflectivity curve from Fig 20 and replotted with ln x-axis. Inset graph shows (left) absorption center peak wavelength and (right) total absorbed light from Gaussian fit functions of the four semilog curves.

Qualitative analysis of Fig 20 clearly shows an improvement in mirror stack reflectivity with decreased ripening time in vacuum between Ag deposition and Ar+ ion bombardment. The absorption feature in the spectra within ~365nm $< \lambda <$ ~500nm, which does not appear in calculated reflectivity of Ag/dielectric simulations, varies in shape and amplitude between the four samples. Quantitative analysis of this absorption feature related to Ag SPR is accomplished by removing the difference in

reflectivity between measured and calculated spectra, applying Gaussian fitting functions to the four curves plotted with ln(wavelength), and extracting trends in Gaussian function characteristics of the four fit curves. Semilog plots of reflectivity curves which have been fit with Gaussian functions are shown in Fig 21, with extracted peak wavelength and total light absorbed (area under curve) for each curve plotted in the bottom right inset. Error bars on data points from the inset in Fig 21 were calculated using systematic measurement error from the Cary 5000 spectrophotometer combined with error from the Gaussian fit to each curve. Both peak wavelength and total area of the absorption feature (reflectivity loss) in the reflectivity spectra appear to have linear dependence on ripening time. The Gaussian fit of the sample exposed to Ar+ ion bombardment after 90 seconds of ripening time shows the least reflectivity loss and lowest (most blue) peak wavelength at ~401nm. The Gaussian fit of the control sample with no direct Ar+ ion exposure shows the most reflectivity loss and the highest peak wavelength at ~405nm.

Observed effects of the Ar+ ion bombardment on Ag/dielectric interfaces are illustrated in Fig 22. As-deposited Ag forms a film with grain size and roughness dependent on deposition mechanism and ambient conditions. The resulting Ag thin film surface morphology continues to evolve over time immediately after deposition at ambient conditions. However, we have shown that exposing Ag thin films to Ar+ ion bombardment somehow slows or inhibits Ag film evolution in vacuum. Upon deposition of further dielectric thin film materials on the Ag surface, the dielectric

film encapsulates and prevents Ag from continuing to evolve and roughen over time. Any roughness and surface features on the Ag prior to dielectric top layer deposition will subsequently affect the optical properties of the Ag/dielectric interface, such as increased scattering and increased coupling efficiency between incident light and SPR modes. Mirrors with Ag immediately exposed to Ar+ ion bombardment remain smooth during subsequent deposition of protective top barrier layers which yields higher reflectivity.

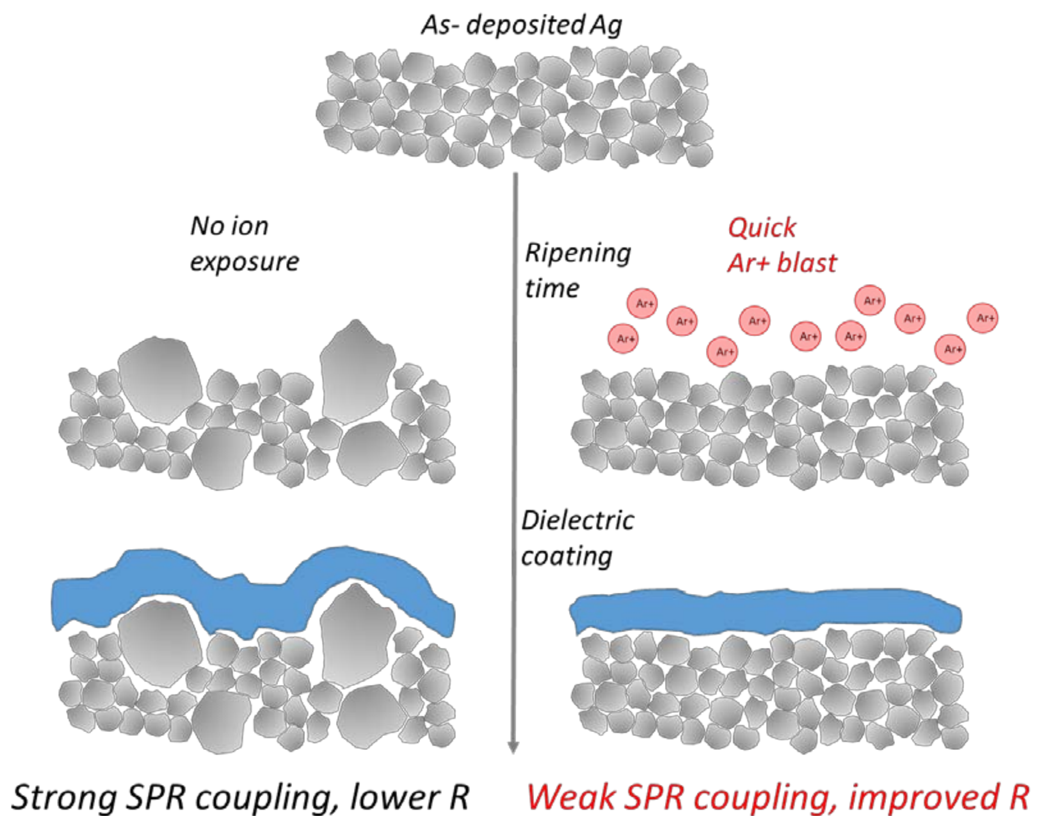

Figure 22: Illustration summarizing the Ag film microstructure (left) without and (right) with 45 seconds Ar+ exposure after Ag film deposition.

Evaporation of noble metals, including Ag, at ambient room temperature has become increasingly popular in thin film applications due to increasing compatibility with semiconductor processing, organic materials, etc. Smooth dense metal films with desirable optical and electrical properties are still obtained at low temperatures relative to the material melting point by also ensuring deposition occurs under high vacuum at relatively fast deposition rates[94]. The homologous temperature, Th, is defined as the ratio of substrate temperature to material melting point, Ts/Tm. With some variation between materials of different reactivity, noble metals deposited with Th < 0.3 in high vacuum (~10-6 or lower) at relatively fast deposition rates (>1nm/second) have been experimentally shown to nucleate and grow within Zone 1 or Zone T as defined by Thornton and Grovenor using the thin film growth structure zone model[95,96]. Metal films that form within Zone 1 typically exhibit small, fibrous grain structure. Zone T growth morphology is described similar to Zone 1 with some dispersion of larger grains when normal grain growth begins to compete with the less mobile self-shadowing mechanism of adatom deposition. Zone 1 growth mode is favorable for metal films in optical or plasmonic applications due to the smooth surface texture and high density formed by small grains. The Ag film surface morphology without ion bombardment shown in Fig 17a and Fig 18a is considered an excellent example of the Zone T growth zone. However, the smoother Ag film exposed to Ar+ ion bombardment shown in Fig 17b and Fig 18b is more indicative of the Zone 1 growth mode with a tighter distribution of smaller grains. The ability for a post-deposition surface treatment to affect the apparent morphological outcome of the

Ag thin film without modifying deposition parameters raises significant questions about the native process of Ag film formation after deposition ends as well as the interaction of positively charged inert ions with the existing Ag surface morphology.

While the structure zone growth model predicts film grain structure and general morphology depending on Th and vacuum level, film structure also depends heavily on deposition rate. Immediately after stopping thin film deposition (deposition rate quickly changes to 0nm/second), adatoms continue to stay mobile across the film surface with residual kinetic energy. Evaporated Ag films have been observed and described by O'Handley et al. to have rapidly reorganizing surface morphology immediately after deposition when studied with in-situ ellipsometry[102]. This surface reorganization, described as a "self-annealing" process, can be explained by the structure zone growth model as a system of adatoms nucleating in vacuum at a certain Th and pressure when deposition rate immediately drops to 0 nm/second. When new adatoms are no longer introduced to the surface, the faster Zone 1 growth mode of fibrous small-grains no longer dominates film formation. Grain growth mechanisms, which may be occurring simultaneously during film nucleation and deposition, continue to influence film formation even after the deposition rate immediately drops to 0 nm/second. Even at substrate temperatures as low as room temperature, freshly-deposited metal thin films continue to evolve and reduce surface energy by surface diffusion. Post-deposition self-annealing at room temperature has been previously observed in Cu and Ag thin films with surface diffusion identified as the primary physical mechanism[102,103]. However, Ag grain growth and surface

diffusion can be inhibited by the presence of alloy impurities[104,105] and adsorbed oxygen or water vapor[106,107]. For the Ag films studied in this work, solid-solution impurities and oxygen/water vapor presence is expected to be negligible.

Albers et al has observed the immediate and residual effects of Ar+ ion bombardment on Ag films in vacuum using ellipsometry. Their results show that the implantation of Ar+ ions significantly changes ellipsometric properties of the bare Ag film during bombardment, and more importantly, for several minutes after bombardment ends[101]. The observed relaxation time in the ellipsometric properties of the Ag film confirm that Ar+ ions are temporarily implanted in the Ag film surface. While Albers et al did not report ellipsometry of Ag films immediately after deposition or Ar+ ion bombardment to the immediately deposited Ag film, we expect that Ar+ ion implantation for 45 seconds on the surface of an immediately deposited Ag film in vacuum significantly interferes with surface diffusion in the self-annealing process. Grain growth of a post-deposited Ag film is inhibited by the temporary presence of residual Ar+ ions. This effect might be described as grain boundary pinning, however, it is unclear whether the small fibrous grains of a Ag film in Zone 1 growth mode actually stop migrating or evolving during subsequent Ar+ ion bombardment. Kinetic energy is undoubtedly added to the Ag surface upon ion bombardment which is expected to contribute to the required energy for any post-deposition self-annealing. We propose that Ar+ ion bombardment of post-deposited Ag films in vacuum suppresses surface diffusion by temporary implantation which inhibits grain growth, despite the increased surface energy expected from ion assisted

processes. While Ar+ ion bombardment may provide sufficient energy for Ag adatoms to overcome the surface diffusion activation energy barrier, we expect the presence of implanted Ar+ ions to cause surface defects and roughen grain boundaries[99,100] and therefore raise the required activation energy of Ag adatom surface diffusion necessary to support grain growth. Because all reflectivity, AFM, and SEM characterization of samples in this study were measured after deposition approximately 2 hours, 12 hours, and 48 hours, respectively, it is evident that the described modified surface morphology is not temporary or immediately reversible. However, we do expect that post-deposition annealing of Ar+ ion bombarded bare Ag samples with suppressed grain growth will result in conventional grain growth and rougher surface morphology.

Ion bombardment of immediately post-deposited Ag films has been shown to enhance optical properties of protected Ag films. However, previous work with the same deposition chamber has shown decreased Ag film reflectivity when deposition is ion-assisted throughout the entire 120nm film thickness[49]. Huang et al have also reported less desirable optical and electrical properties of Ag films deposited with ion assist when compared to evaporation without any ions. Decreased optical and electrical conductivity of ion-assisted evaporated Ag films are explained by the de-densification and void formation within the Ag films due to the limited range of Ag surface diffusion[108,109]. While surface diffusion suppression by Ar+ ions is not beneficial to Ag film properties within the "bulk" of the film, this work suggests that the same mechanism of suppressing surface diffusion post-deposition with a short

Ar+ ion exposure increases Ag reflectivity, specifically when SPR absorption due to protective dielectric overlayers is considered. It should be noted that excessive ex-situ Ar+ ion bombardment of Ag films has been shown to significantly damage Ag grains[99,100]. Dobrev observes anisotropic implantation and defect formation of Ag grains by Ar+ ion bombardment which results in (110) planes preferentially forming in contrast to the more commonly observed (111) plane[99]. While a short exposure of this effect on Ag film surfaces may be optically beneficial, such as the 45 second ion exposure in this work, excessive Ar+ ion bombardment is expected to eventually be detrimental to Ag optical properties.

7.1 Conclusion

Silver-based mirrors were designed and deposited with the introduction of an Ar+ ion bombarding technique on the as-deposited Ag surface prior to subsequent deposition of protective top barrier layers. Increased reflectivity in the UV/visible spectrum was achieved by exposing Ag films to Ar+ ions. SEM and AFM characterization of bare Ag films reveals that bare Ag exposed to Ar+ ions is smoother with smaller grains while as-deposited Ag exhibits a wider distribution of grain size with sharper features and increased roughness. We propose that Ar+ ion exposure slows or inhibits a native process of Ag thin film self-annealing by surface diffusion at ambient conditions in vacuum. After deposition of a protective dielectric coating on Ag, optical losses due to Ag/dielectric interface morphology, namely SPR absorption, are shown in reflectivity measurements. Mirrors deposited with varying

lengths of idle time in vacuum between Ag film deposition and Ar+ ion bombardment confirms that highest blue spectrum reflectivity is achieved by immediate post-Ag exposure to Ar+ ions. Further investigation is necessary to understand the physical mechanisms between Ar+ ions and Ag thin film surfaces responsible for the observed suppression of Ag diffusion and evolution.

Chapter 8

Conclusion

The ALD process has been demonstrated as a thin film deposition technique for a variety of diverse applications. Each application has benefitted from the specific and unique properties of the ALD film growth process. Utilizing a cycle of discrete steps forming self-limiting chemistry within the ALD growth window of the CVD process, it is possible to obtain precise thickness high quality amorphous thin films devoid of pinholes and defects. Deposited films also uniformly coat every substrate surface of complex geometries and high-aspect ratio features with conformal coverage. These unique growth properties are virtually impossible to achieve with other thin film deposition mechanisms for dielectric materials. Therefore, ALD was used to deposit dielectric films for the specific applications which rely upon these unique deposition properties.

Indium phosphide semiconductor nanowire networks were coated with various thicknesses of AlOx using PEALD. The complex 3-dimentional network formed by randomly oriented nanowires was conformally covered with a uniform layer of AlOx, and optoelectronic properties of the nanowire networks were analyzed.

AlOx thickness is correlated to a blue-shift in the photoluminescence of the semiconductor nanowire networks due to fixed surface charge inherent in the AlOx coating shell which is uniformly distributed around each nanowire circumference.

Novel memristor “edge” devices were fabricated with conventional photolithography patterning of top and bottom electrodes deposited by e-beam evaporation and an active switching layer of titanium dioxide deposited by PEALD. Device IV curves were measured, and device structure was analyzed by cross-sectional SEM imaging. The conformal ALD thin film switching layer is necessary to uniformly and consistently cover the sidewall junctions between the top and bottom electrodes to prevent shorting. This “edge” fabrication technique yields an active device cross-section two orders of magnitude smaller than what is possible with conventional 2-dimensional thin film devices fabricated by similar photolithography methods.

Highly reflective thin film silver mirrors were coated with protective dielectric barrier overlayers such as AlOx, hafnium oxide, and titanium dioxide by ALD and plasma-enhanced ALD. Protected mirrors were tested in an accelerated environmental stressing chamber, and reflectivity and durability were analyzed to determine the most overall effective barrier materials. When comparing mirrors coated with identical layers of AlOx deposited by conventional e-beam evaporation vs. PEALD, mirrors with AlOx deposited by PEALD showed superior barrier properties. Success of the ALD barriers are attributed to the conformal, pinhole-free nature of the deposition process; the same defect- and pinhole-free coverage is not easily attained

by conventional physical vapor deposition methods. A figure of merit is proposed to quantitatively assess overall mirror performance by combining stress testing durability and reflectivity analysis.

In the interest of depositing dielectric barrier overlayers by ALD directly onto bare Ag while retaining high-quality optical properties, the surface morphology of Ag films was studied in relation to SPR absorption enhanced by the presence of subsequent dielectric barrier overlayers. Ag surface morphology was modified by an immediate post-deposition argon ion bombardment technique to produce optically favorable smoother silver surfaces with smaller grains and therefore lower SPR absorption. This SPR-reducing surface treatment technique yields higher mirror reflectivity after dielectric barrier overlayers are deposited.

Bibliography

[1] Secula, Erik. "Thin Film Electronics." (2014).

[2] Tummala, Rao, et al. "Thin-film packaging." Microelectronics Packaging Handbook. Springer US, 1997. 624-813.

[3] Jackson, Thomas N., et al. "Organic thin-film transistors for organic light-emitting flat-panel display backplanes." IEEE Journal of selected topics in quantum electronics 4.1 (1998): 100-104.

[4] Sproul, William D. "Physical vapor deposition tool coatings." Surface and Coatings Technology 81.1 (1996): 1-7.

[5] De Azeredo, Henriette MC. "Nanocomposites for food packaging applications." Food Research International 42.9 (2009): 1240-1253.

[6] Park, Jong-Hee, and T. S. Sudarshan, eds. Chemical vapor deposition. Vol. 2. ASM international, 2001.

[7] Dahal, R., et al. "InGaN/GaN multiple quantum well solar cells with long operating wavelengths." Applied Physics Letters 94.6 (2009): 063505.

[8] Mo, Chunlan, et al. "Growth and characterization of InGaN blue LED structure on Si (111) by MOCVD." Journal of crystal growth 285.3 (2005): 312-317.

[9] Palacios, T., et al. "High-power AlGaN/GaN HEMTs for Ka-band applications." IEEE Electron Device Letters 26.11 (2005): 781-783.

[10] George, Steven M. "Atomic layer deposition: an overview." Chemical reviews 110.1 (2009): 111-131.

[11] Leskelä, Markku, and Mikko Ritala. "Atomic layer deposition (ALD): from precursors to thin film structures." Thin solid films 409.1 (2002): 138-146.

[12] Yu, Heng, et al. "Two-versus three-dimensional quantum confinement in indium phosphide wires and dots." Nature materials 2.8 (2003): 517-520.

[13] Samuelson, Lars, et al. "Semiconductor nanowires for 0D and 1D physics and applications." Physica E: Low-dimensional Systems and Nanostructures 25.2 (2004): 313-318.

[14] Lohn, Andrew J., et al. "Morphological Effect of Doping Environment on Silicon Nanowires Grown by Plasma-Assisted Chemical Vapor Deposition." Japanese Journal of Applied Physics 51.11S (2012): 11PE04.

[15] Norris, Kate J., et al. "Indium phosphide nanowire network: growth and characterization for thermoelectric conversion." SPIE NanoScience+ Engineering. International Society for Optics and Photonics, 2012.

[16] Gudiksen, Mark S., Jianfang Wang, and Charles M. Lieber. "Size-dependent photoluminescence from single indium phosphide nanowires." The Journal of Physical Chemistry B 106.16 (2002): 4036-4039.

[17] Colombo, C., et al. "Ga-assisted catalyst-free growth mechanism of GaAs nanowires by molecular beam epitaxy." Physical Review B 77.15 (2008): 155326.

[18] Chuang, Linus C., et al. "Critical diameter for III-V nanowires grown on lattice-mismatched substrates." Applied Physics Letters 90.4 (2007): 043115.

[19] Lohn, Andrew J., Xuema Li, and Nobuhiko P. Kobayashi. "Epitaxial growth of ensembles of indium phosphide nanowires on various non-single crystal substrates using an amorphous template layer." Journal of Crystal Growth 315.1 (2011): 157-159.

[20] Chua, Leon. "Memristor-the missing circuit element." IEEE Transactions on circuit theory 18.5 (1971): 507-519.

[21] Chua, Leon O., and Sung Mo Kang. "Memristive devices and systems." Proceedings of the IEEE 64.2 (1976): 209-223.

[22] Xia, Qiangfei. "Nanoscale resistive switches: devices, fabrication and integration." Applied Physics A 102.4 (2011): 955-965.

[23] Vontobel, Pascal O., et al. "Writing to and reading from a nano-scale crossbar memory based on memristors." Nanotechnology 20.42 (2009): 425204.

[24] Yang, J. Joshua, Dmitri B. Strukov, and Duncan R. Stewart. "Memristive devices for computing." Nature nanotechnology 8.1 (2013): 13-24.

[25] Xia, Qiangfei, et al. "Memristor− CMOS hybrid integrated circuits for reconfigurable logic." Nano letters 9.10 (2009): 3640-3645.

[26] Jo, Sung Hyun, et al. "Nanoscale memristor device as synapse in neuromorphic systems." Nano letters 10.4 (2010): 1297-1301.

[27] Chen, An, et al. "Non-volatile resistive switching for advanced memory applications." IEEE InternationalElectron Devices Meeting, 2005. IEDM Technical Digest. IEEE, 2005.

[28] Strukov, Dmitri B., et al. "The missing memristor found." nature 453.7191 (2008): 80-83.

[29] Choi, Byung Joon, et al. "New materials for memristive switching." 2014 IEEE International Symposium on Circuits and Systems (ISCAS). IEEE, 2014.

[30] Choi, Byung Joon, et al. "Electrical performance and scalability of Pt dispersed SiO2 nanometallic resistance switch." Nano letters 13.7 (2013): 3213-3217.

[31] Chua, Leon. "If it’s pinched it’sa memristor." Semiconductor Science and Technology 29.10 (2014): 104001.

[32] Miao, Feng, et al. "Anatomy of a Nanoscale Conduction Channel Reveals the Mechanism of a High‐Performance Memristor." Advanced materials 23.47 (2011): 5633-5640.

[33] Strachan, John Paul, et al. "Direct identification of the conducting channels in a functioning memristive device." Advanced Materials 22.32 (2010): 3573-3577.

[34] Yang, J. Joshua, et al. "Metal/TiO2 interfaces for memristive switches." Applied Physics A 102.4 (2011): 785-789.

[35] Gergel-Hackett, Nadine, et al. "A flexible solution-processed memristor." IEEE Electron Device Letters 30.7 (2009): 706-708.

[36] Duraisamy, Navaneethan, et al. "Fabrication of TiO 2 thin film memristor device using electrohydrodynamic inkjet printing." Thin Solid Films 520.15 (2012): 5070-5074.

[37] Xia, Qiangfei, et al. "Self-aligned memristor cross-point arrays fabricated with one nanoimprint lithography step." Nano letters 10.8 (2010): 2909-2914.

[38] Gale, Ella. "TiO2-based memristors and ReRAM: materials, mechanisms and models (a review)." Semiconductor Science and Technology 29.10 (2014): 104004.

[39] Yang, J. Joshua, et al. "Diffusion of adhesion layer metals controls nanoscale memristive switching." Advanced materials 22.36 (2010): 4034-4038.

[40] Yang, J. Joshua, et al. "The mechanism of electroforming of metal oxide memristive switches." Nanotechnology 20.21 (2009): 215201.

[41] Baek, I. G., et al. "Realization of vertical resistive memory (VRRAM) using cost effective 3D process." Electron Devices Meeting (IEDM), 2011 IEEE International. IEEE, 2011.

[42] Chien, W. C., et al. "Multi-layer sidewall WO x resistive memory suitable for 3D ReRAM." VLSI Technology (VLSIT), 2012 Symposium on. IEEE, 2012.

[43] Yu, Shimeng, et al. "HfOx-based vertical resistive switching random access memory suitable for bit-cost-effective three-dimensional cross-point architecture." ACS nano 7.3 (2013): 2320-2325.

[44] Hsu, Chung-Wei, et al. "3D Vertical TaOx/TiO2 RRAM with over 10 (3) Self-Rectifying Ratio and Sub-mu A Operating Current." 2013 IEEE INTERNATIONAL ELECTRON DEVICES MEETING (IEDM). 2013.

[45] Jacobson, Michael R., et al. "Development of silver coating options for the Gemini 8-m telescopes project." Astronomical Telescopes & Instrumentation. International Society for Optics and Photonics, 1998.

[46] Boccas, Maxime, et al. "Coating the 8-m Gemini telescopes with protected silver." SPIE Astronomical Telescopes+ Instrumentation. International Society for Optics and Photonics, 2004.

[47] Vucina, Tomislav, et al. "Gemini primary mirror in situ wash." SPIE Astronomical Telescopes+ Instrumentation. International Society for Optics and Photonics, 2008.

[48] Phillips, Andrew C., et al. "Progress toward high-performance reflective and anti-reflection coatings for astronomical optics." SPIE Astronomical Telescopes+ Instrumentation. International Society for Optics and Photonics, 2008.

[49] Phillips, Andrew C., et al. "Progress toward high-performance astronomical coatings." SPIE Astronomical Telescopes+ Instrumentation. International Society for Optics and Photonics, 2010.

[50] Phillips, Andrew C., et al. "Progress in UCO's search for silver-based telescope mirror coatings." SPIE Astronomical Telescopes+ Instrumentation. International Society for Optics and Photonics, 2012.

[51] "TMT Design Requirements Document for Telescope Optical Coatings" (http://www.tmt.org/sites/default/files/documents/application/pdf/design-req-for-optical-coatings%2020111109.pdf)

[52] Casey Jr, H. C., and E. Buehler. "Evidence for low surface recombination velocity on n - type InP." Applied Physics Letters 30.5 (1977): 247-249.

[53] Lohn, Andrew J., et al. "Study on indium phosphide nanowires grown by metal organic chemical vapor deposition and coated with aluminum oxides deposited by atomic layer deposition." SPIE NanoScience+ Engineering. International Society for Optics and Photonics, 2012.

[54] Kobayashi, Nobuhiko P., et al. "Growth and characterization of indium phosphide single-crystal nanoneedles on microcrystalline silicon surfaces." Applied Physics A 85.1 (2006): 1-6.

[55] Mattila, M., et al. "Crystal-structure-dependent photoluminescence from InP nanowires." Nanotechnology 17.6 (2006): 1580.

[56] Murayama, M., and T. Nakayama. "Chemical trend of band offsets at wurtzite/zinc-blende heterocrystalline semiconductor interfaces." Physical Review B 49.7 (1994): 4710.

[57] Cox, J. D., Donald D. Wagman, and Vadim Andreevich Medvedev. CODATA key values for thermodynamics. Chem/Mats-Sci/E, 1989.

[58] Miikkulainen, Ville, et al. "Crystallinity of inorganic films grown by atomic layer deposition: Overview and general trends." Journal of Applied Physics 113.2 (2013): 021301.

[59] Montazeri, Mohammad, et al. "Direct Measure of Strain and Electronic Structure in GaAs/GaP Core− Shell Nanowires." Nano letters 10.3 (2010): 880-886.

[60] Agostinelli, G., et al. "Very low surface recombination velocities on p-type silicon wafers passivated with a dielectric with fixed negative charge." Solar Energy Materials and Solar Cells 90.18 (2006): 3438-3443.

[61] Shin, Byungha, et al. "Origin and passivation of fixed charge in atomic layer deposited aluminum oxide gate insulators on chemically treated InGaAs substrates." Applied physics letters 96.15 (2010): 152908.

[62] Giessen, H., et al. "Observation of the quantum confined ground state in InP quantum dots at 300 K." Applied physics letters 68.3 (1996): 304-306.

[63] Grundmann, Marius. The Physics of Semiconductors: An Introduction Including Nanophysics and Applications. Springer, 2016.

[64] Liu, C., et al. "Blueshift of electroluminescence from single n-InP nanowire/p-Si heterojunctions due to the Burstein? Moss effect." Nanotechnology 19.46 (2008): 465203.

[65] Zheng, H. Q., et al. "Metamorphic InP/InGaAs double-heterojunction bipolar transistors on GaAs grown by molecular-beam epitaxy." Applied Physics Letters 77 (2000): 869.

[66] Sieg, R. M., and S. A. Ringel. "Reabsorption, band - gap narrowing, and the reconciliation of photoluminescence spectra with electrical measurements for epitaxial n - InP." Journal of applied physics 80.1 (1996): 448-458.

[67] Yao, S. K. "Theoretical model of thin - film deposition profile with shadow effect." Journal of Applied Physics 50.5 (1979): 3390-3395.

[68] Jousten, Karl, ed. Handbook of vacuum technology. John Wiley & Sons, 2008.

[69] Yang, J. Joshua, et al. "Dopant control by atomic layer deposition in oxide films for memristive switches." Chemistry of Materials 23.2 (2010): 123-125.

[70] Yang, J. Joshua, et al. "Memristive switching mechanism for metal/oxide/metal nanodevices." Nature nanotechnology 3.7 (2008): 429-433.

[71] Phillips, Andrew C., et al. "Progress and new techniques for protected-silver coatings." SPIE Astronomical Telescopes+ Instrumentation. International Society for Optics and Photonics, 2014.

[72] Barrie, James D., et al. "Control of stress in protected silver mirrors prepared by plasma beam sputtering." Applied optics 50.9 (2011): C135-C140.

[73] Chu, Chung-Tse, Peter D. Fuqua, and James D. Barrie. "Corrosion characterization of durable silver coatings by electrochemical impedance spectroscopy and accelerated environmental testing." Applied optics 45.7 (2006): 1583-1593.

[74] Jobst, Paul Johannes, et al. "Optical properties of unprotected and protected sputtered silver films: Surface morphology vs. UV/VIS reflectance." Advanced Optical Technologies 3.1 (2014): 91-102.

[75] Phillips, Andrew C., et al. "Fluoride damage to substrates during stripping of mirrors." SPIE Astronomical Telescopes+ Instrumentation. International Society for Optics and Photonics, 2014.

[76] von Seefeld, H. E. R. M. A. N. N., et al. "Investigation of titanium—nitride layers for solar-cell contacts." IEEE Transactions on Electron Devices 27.4 (1980): 873-876.

[77] Bennett, H. E., and J. L. Stanford. "Structure-related optical characteristics of thin metallic films in the visible and ultraviolet." Standardization in Spectrophotometry and Luminescence Measurements: Proceedings of a Workshop Seminar Held at the National Bureau of Standards, Gaithersburg, Maryland, November, November 19-20, 1975. Vol. 466. US Department of Commerce, National Bureau of Standards, 1976.

[78] Martin, P. J. "Ion-based methods for optical thin film deposition." Journal of materials science 21.1 (1986): 1-25.

[79] Cimalla, V., et al. "Densification of thin aluminum oxide films by thermal treatments." Materials Sciences and Applications 5.08 (2014): 628.

[80] Cibert, C., et al. "Properties of aluminum oxide thin films deposited by pulsed laser deposition and plasma enhanced chemical vapor deposition." Thin Solid Films 516.6 (2008): 1290-1296.

[81] Wefers, Karl, and Chanakya Misra. "Oxides and hydroxides of aluminum." (1987).

[82] Schwinde, Stefan, et al. "Description of particle induced damage on protected silver coatings." Applied optics 54.16 (2015): 4966-4971.

[83] León, Juan J. Díaz, et al. "Aluminum titanium oxide alloys: Deposition of amorphous, transparent, corrosion-resistant films by pulsed DC reactive magnetron sputtering with RF substrate bias." Materials Science in Semiconductor Processing 36 (2015): 96-102.

[84] Gao, Xiao-Yong, et al. "Study of structure and optical properties of silver oxide films by ellipsometry, XRD and XPS methods." Thin Solid Films 455 (2004): 438-442.

[85] Abràmoff, Michael D., Paulo J. Magalhães, and Sunanda J. Ram. "Image processing with ImageJ." Biophotonics international 11.7 (2004): 36-42.

[86] Shou-Yong, Jing, et al. "Investigation on lattice constants of Mg-Al spinels." Journal of materials science letters 19.3 (2000): 225-227.

[87] Perry, A. J. "The relationship between residual stress, X-ray elastic constants and lattice parameters in TiN films made by physical vapor deposition." Thin Solid Films 170.1 (1989): 63-70.

[88] James, M. A., and T. Hibma. "Thickness-dependent relaxation of NiO (001) overlayers on MgO (001) studied by X-ray diffraction." Surface science 433 (1999): 718-722.

[89] Hermann, Klaus. Crystallography and Surface Structure: An Introduction for Surface Scientists and Nanoscientists. John Wiley & Sons, 2011.

[90] Rycenga, Matthew, et al. "Understanding the SERS effects of single silver nanoparticles and their dimers, one at a time." The journal of physical chemistry letters 1.4 (2010): 696-703.

[91] Bennett, H. E., and J. L. Stanford. "Structure-related optical characteristics of thin metallic films in the visible and ultraviolet." Standardization in Spectrophotometry and Luminescence Measurements: Proceedings of a Workshop Seminar Held at the National Bureau of Standards, Gaithersburg, Maryland, November, November 19-20, 1975. Vol. 466. US Department of Commerce, National Bureau of Standards, 1976.

[92] Braundmeier, A. J., and E. T. Arakawa. "Effect of surface roughness on surface plasmon resonance absorption." Journal of Physics and Chemistry of Solids 35.4 (1974): 517-520.

[93] Stanford, J. L., and H. E. Bennett. "Enhancement of surface plasma resonance absorption in mirrors by overcoating with dielectrics." Applied optics 8.12 (1969): 2556-2557.

[94] McPeak, Kevin M., et al. "Plasmonic films can easily be better: rules and recipes." ACS photonics 2.3 (2015): 326-333.

[95] Grovenor, C. R. M., H. T. G. Hentzell, and D. A. Smith. "The development of grain structure during growth of metallic films." Acta Metallurgica 32.5 (1984): 773-781.

[96] Thornton, John A. "The microstructure of sputter ‐ deposited coatings." Journal of Vacuum Science & Technology A 4.6 (1986): 3059-3065.

[97] Osman, Maged A., and Beat A. Keller. "Wettability of native silver surfaces." Applied surface science 99.3 (1996): 261-263.

[98] Negri, Pierre, et al. "Removal of surface contamination and self-assembled monolayers (SAMs) from silver (Ag) nanorod substrates by plasma cleaning with argon." Applied spectroscopy 65.1 (2011): 66-74.

[99] Dobrev, D. "Ion-beam-induced texture formation in vacuum-condensed thin metal films." Thin Solid Films 92.1 (1982): 41-53.

[100] Ogilvie, G. J. "The surface structure of silver crystals after argon-ion bombardment." Journal of Physics and Chemistry of Solids 10.2 (1959): 222-228.

[101] Albers, H., J. M. M. Droog, and G. A. Bootsma. "Ellipsometric study of the effect of argon ion Bombardment on the structure and reactivity of Ag (111)." Surface Science 64.1 (1977): 1-22.

[102] O'handley, R. C., et al. "Residual gas and the optical properties of silver films." Surface Science 50.2 (1975): 407-433.

[103] Harper, J. M. E., et al. "Mechanisms for microstructure evolution in electroplated copper thin films near room temperature." Journal of applied physics 86.5 (1999): 2516-2525.

[104] Adamik, M., P. B. Barna, and I. Tomov. "Correlation between texture and average grain size in polycrystalline Ag thin films." Thin Solid Films 359.1 (2000): 33-38.

[105] Holm, Elizabeth A., and Stephen M. Foiles. "How grain growth stops: A mechanism for grain-growth stagnation in pure materials." Science 328.5982 (2010): 1138-1141.

[106] Rhead, G. E. "Surface self-diffusion of silver in various atmospheres." Acta metallurgica 13.3 (1965): 223-226.

[107] Yoshihara, Kazuhiro, and Kazuyoshi Nii. "The effect of oxygen potential on the surface self-diffusion coefficient of silver." Transactions of the Japan Institute of Metals 20.9 (1979): 533-542.

[108] Huang, T. C., et al. "Effect of ion bombardment during deposition on the x‐ray microstructure of thin silver films." Journal of Vacuum Science & Technology A 3.6 (1985): 2161-2166.

[109] Parmigiani, F., et al. "Optical and electrical properties of thin silver films grown under ion bombardment." Physical Review B 33.2 (1986): 879.